Summer 2018

# Direct printing of single-crystal silicon by microscale nanoparticle printing and confined laser melting and crystallization

Wan Shou

Department: Mechanical and Aerospace Engineering

## Recommended Citation

Shou, Wan, "Direct printing of single-crystal silicon by microscale nanoparticle printing and confined laser melting and crystallization" (2018). *Doctoral Dissertations*. 2898.
https://scholarsmine.mst.edu/doctoral_dissertations/2898

# DIRECT PRINTING OF SINGLE-CRYSTAL SILICON BY MICROSCALE NANOPARTICLE PRINTING AND CONFINED LASER MELTING AND CRYSTALLIZATION

by

WAN SHOU

Presented to the Faculty of the Graduate School of the

MISSOURI UNIVERSITY OF SCIENCE AND TECHNOLOGY

In Partial Fulfillment of the Requirements for the Degree

DOCTOR OF PHILOSOPHY

in

MECHANICAL ENGINEERING

2018

Approved by:

Dr. Heng Pan, Advisor
Dr. Hai-lung Tsai
Dr. Frank Liou
Dr. Ming Leu
Dr. Joseph W Newkirk

# PUBLICATION DISSERTATION OPTION

This dissertation consists of the following three articles that have been published or submitted for publication as follows:

Paper I, “Silicon-wall Interfacial Free Energies via Thermodynamics Integration” has been published in The Journal of Chemical Physics and can be found on pages 5-37.

Paper II, “Transport and Interfacial Phenomena in Nanoscale Confined Laser Crystallization” has been published in proceedings of ASME 2017 12th International Manufacturing Science and Engineering Conference collocated with the JSME/ASME 2017 6th International Conference on Materials and Processing. It can be found on pages 38-56.

Paper III, “Direct Printing Single-crystal Si Islands by Microscale Nanoparticle Printing and Confined Laser Melting and Crystallization” is intended for submission to ACS Nano and can be found on pages 57-84.

# ABSTRACT

The transport and interfacial phenomena in laser melting and crystallization of silicon in micro-/nano-scale confinement lacks sufficient understanding. Uncovering the underlying mechanisms, and hence harness the melting and crystallization processes can help the formation of controllable single-crystal structures or patterns. In this dissertation, a molecular dynamics (MD) simulation was conducted to calculate the interfacial free energy of the silicon system in contact with flat and structured walls. Then the calculated interfacial energies were employed to predict the nucleation mechanisms in a slab of liquid silicon confined by two walls and compared with MD simulation results. Further, in combination with a macroscopic model, it was concluded that for a given domain size, longer laser pulse increases the probability of forming single crystals. It was also suggested that for micro size Si domains, a continuous wave (CW) laser operated in a scanning mode can possibly generate single crystal structure.

To examine the theoretical predication, CW laser crystallization of Si nanoparticles was conducted. A non-vacuum printing process, aerosol printing, was adopted in this dissertation, which enabled us to prepare Si film and lines with a cost-effective manner. Followed with pressing, the Si nanoparticles were densified and planarized. Then, the nanoparticles were laser melted and crystallized in the confined domain. It was found that the morphology and crystalline structure can be modulated from poly-crystal line to single-crystal islands through tuning the gap of confinement.

# ACKNOWLEDGMENTS

First and foremost, I would like to express my sincere gratitude to my advisor, Dr. Heng Pan, for his encouragement, insightful guidance, and support during my PhD study at Missouri University of Science and Technology. Without him, I could not move step by step toward my defense and dissertation. He patiently guided me through every stage of my research meanwhile leaving me sufficient freedom to think independently. His encouragement gave me confidence to continue exploring unknown scientific territory and challenging myself to be the best. His diligence and rigorous altitude to research and work has a significant influence on my research and will continue influencing my future academic life. It has been a great honor to work with him for pursuing my PhD degree.

I would also like to extend my appreciation to all my dissertation committee members, Dr. Hai-lung Tsai, Dr. Frank Liou, Dr. Ming Leu, and Dr. Joseph W Newkirk. Without their guidance and valuable comments, it is impossible for me to complete my dissertation.

I would like to express my deep thanks to my groupmates and friends, especially, Mr. Brandon Ludwig, Ms. Xiaowei Yu, Mr. Joshua Staggs, Mr. Chinmoy Podder, Mr. Bikram Mahajan, Mr. Xiangtao Gong, and Mr. Letian Wang for their support during my study in Rolla.

Last but not the least, I wish to extend my special and sincere thanks to my parents, my wife, daughter, and all other family members, for their love and unwavering support.

## TABLE OF CONTENTS

Page

PUBLICATION DISSERTATION OPTION .................................................................. iii

ABSTRACT................................................................................................................ iv

ACKNOWLEDGMENTS .............................................................................................. v

LIST OF ILLUSTRATIONS.......................................................................................... ix

LIST OF TABLES ........................................................................................................ xi

SECTION

1. INTRODUCTION.................................................................................................... 1

1.1. BACKGROUND.................................................................................................. 1

1.2. RESEARCH OBJECTIVES................................................................................ 2

1.3. ORGANIZATION OF DISSERTATION............................................................. 3

PAPER

I. SILICON-WALL INTERFACIAL FREE ENERGY VIA THERMODYNAMICS INTEGRATION.................................................................................................... 5

ABSTRACT............................................................................................................. 6

1. INTRODUCTION ................................................................................................. 6

2. MODEL POTENTIAL............................................................................................ 9

3. CALCULATION OF INTERFACIAL FREE ENERGIES ...................................... 12

3.1. HAMILTONIAN, PARTITION FUNCTIONS AND GIBBS FREE ENERGY...................................................................................................... 12

3.2. PARAMETRIZATION WITH Λ AND INTERFACIAL ENERGY CALCULATED BY TI ....................................................................... 13

3.3. INTERFACIAL FREE ENERGY CALCULATED BY PRESSURE ANISOTROPY ........ 17

4. BOP COMPUTATION ........ 18

5. SIMULATION DETAILS ........ 19

6. RESULTS ........ 24

6.1. LIQUID-FLAT WALL INTERFACIAL ENERGY ........ 24

6.2. SOLID-FLAT WALL INTERFACIAL ENERGY ........ 26

6.3. CRYSTALLIZATION ON FLAT WALLS ........ 29

6.4. LIQUID SI-SIO$_2$ WALL AND SOLID SI-SIO$_2$ WALL INTERFACIAL ENERGY ........ 30

6.5. CRYSTALLIZATION ON SIO$_2$ WALLS ........ 32

7. CONCLUSION ........ 33

ACKNOWLEDGMENTS ........ 34

REFERENCES ........ 34

II. TRANSPORT AND INTERFACIAL PHENOMENA IN NANOSCALE CONFINED LASER CRYSTALLIZATION ........ 38

ABSTRACT ........ 38

1. INTRODUCTION ........ 39

2. METHOD ........ 42

2.1. TRANSPORT IN NANO-CONFINED CRYSTALLIZATION ........ 42

2.2. INTERFACIAL ENERGIES OF SI-SIO$_2$ INTERFACES ........ 45

3. RESULTS ........ 47

3.1. TRANSPORT IN NANO-CONFINED CRYSTALLIZATION ........ 47

3.2. INTERFACIAL ENERGIES OF SI-SIO$_2$ INTERFACES ........ 51

4. CONCLUSIONS ........ 53
ACKNOWLEDGEMENTS ........ 54
REFERENCES ........ 54
III. DIRECT PRINTING SINGLE-CRYSTAL SI ISLANDS BY MICROSCALE NANOPARTICLE PRINTING AND CONFINED LASER MELTING AND CRYSTALLIZATION ........ 57
ABSTRACT ........ 57
1. INTRODUCTION ........ 57
2. RESULTS AND DISCUSSION ........ 60
3. CONCLUSIONS ........ 69
4. MATERIALS AND METHODS ........ 69
ACKNOWLEDGEMENTS ........ 70
REFERENCES ........ 71
SUPPLEMENTAL INFORMATION ........ 79

SECTION

2. CONCLUSIONS ........ 85
3. FUTURE WORK ........ 87
REFERENCES ........ 89
VITA. ........ 91

## LIST OF ILLUSTRATIONS

Page

PAPER I

Figure 1. MD simulation configuration and the two-step thermodynamic integration scheme ........ 20

Figure 2. The interfacial configuration between Si and $SiO_2$ (up) and selected Si crystal surfaces (down) ........ 23

Figure 3. The thermodynamic integrand during TI steps ........ 24

Figure 4. The interfacial energies between liquid Si and flat walls for different confining pressure (a) and temperature (b); Calculated normal and tangential pressure components under 1000 bar (c) and 5000 bar (d) confining pressures ........ 25

Figure 5. (a) The interfacial energies between solid Si (111) and flat walls for different temperatures; (b) The interfacial energies of liquid-wall and solid-wall near melting temperature under different confining pressures ........ 27

Figure 6. The interfacial energies between different orientated Si crystals with flat wall ........ 28

Figure 7. The distribution of nucleus in the slab under different confining pressures ..... 29

Figure 8. The thermodynamic integrand during TI step 2-flat wall to $SiO_2$ wall transition for liquid-Si (a) and solid-Si (b) interfaces; (c) Direct simulated dewetting of liquid Si on $SiO_2$ substrate ........ 31

Figure 9. The location and size of the largest cluster during the cooling simulation of unconfined slab (a) and $SiO_2$ wall confined slab (b); (c) The crystalline structure at the solid Si-$SiO_2$ interface. ........ 33

PAPER II

Figure 1. Illustrations of the free-standing droplet and wall-confined droplet.…………43

Figure 2. MD simulation configuration and the two-step thermodynamic integration scheme. ........ 45

Figure 3. (a-d) Time-resolved MD snapshots to illustrate initial crystal growth in wall-confined droplets; (e) The comparison of temperature rises (as a result of latent heat release) between free-standing droplets and wall-confined droplets. ........ 48

Figure 4. Validation of the phenomenogical model with MD simulation for wall-confined droplets. ........ 49

Figure 5. The predictions by the phenomenogical model to evaluate the effects of pulsed laser width on the single crystal formations........ 50

Figure 6. The thermodynamic integrand during TI step 2-flat wall to $SiO_2$ wall transition for liquid-Si (a) and solid-Si (b) interfaces; (c) Direct simulated liquid Si droplet on $SiO_2$ substrate........ 52

PAPER III

Figure 1. (a) Conceptual design of laser direct writing of crystalline nano-ribbon in confinement: i. Aerosol printing of microscale pattern using Si NPs; ii. Pressing and confined laser crystallization; iii. Transfer print of fabricated Si to flexible substrate; (b) Representative photographs of printed Si pattern: i. The smallest continuous line; ii. Wafer scale printing; (c) Detailed procedures for single-crystal Si ribbon manufacturing: (i) Densify/planarize of printed Si NPs; (ii) Laser melting/break-up of printed NPs; (iii)(iv) Single crystal nucleation and growth; (v) Disassembly and etching of single-crystal ribbons array; (vi) Transfer of crystalline Si ribbon to flexible substrate. ........ 61

Figure 2. The influence of pressing-assisted confining on sintering of Si nanoparticles.... ........ 62

Figure 3. Influence of confining gap on the morphology and crystalline structure of annealed Si........ 66

Figure 4. Transfer of fabricated single-crystal Si islands. ........ 68

# LIST OF TABLES

Page

PAPER I

Table 1. Tersoff potential based parameters for Si-O system........................................... 11

Table 2. The simulation dimensions for TI calculation of solid Si with confining walls..23

# SECTION

## 1. INTRODUCTION

### 1.1. BACKGROUND

Laser crystallization of amorphous silicon film has been widely studied for decades [1-9], however, the interfacial phenomena during melting and solidification need to be elucidated, especially the nucleation mechanism of Si in contact with different substrates (such as silicon oxide, silicon nitrate and quartz). It is known that the preferred crystal growth scenario is continuous growth from the solidified region of the crystal without new nucleation sites at the substrate, which will maximize the crystalline grain size. Such directional solidification process is sought in laser manufacturing of high quality Si (e.g. polycrystalline or single-crystalline). In addition, the interaction of liquid-substrate will also affect the orientation of the crystal [10].

In order to predict the nucleation behavior, starting from interface (heterogeneous nucleation) or interior (homogeneous nucleation), it is necessary to know the value of ($\gamma_{cs}$-$\gamma_{ls}$) and $\gamma_{lc}$, where $\gamma_{cs}$ is the interfacial energy between crystal and substrate, $\gamma_{ls}$ is the interfacial energy between liquid and substrate, and $\gamma_{lc}$ is the interfacial energy between liquid and crystal. Here, the value of $\gamma_{lc}$ has been extensively studied both theoretically and experimentally, and is relatively easy to access, although in a wide range from 0.167 to 0.43 $J/m^2$[11-18]. However, the interfacial energies between Si and $SiO_2$ substrate (both crystal Si-$SiO_2$ and liquid Si-$SiO_2$) are more difficult to obtain, and there is no systematic study of Si-$SiO_2$ interfaces.

On the other hand, the manufacturing of single crystal Si mainly relies on Czochralski (Cz) growth method [19]. In order to fabricate semiconductor devices from single crystals, expensive lithographic processing [20,21] and vacuum based vapor-liquid-solid growth approaches [22,23] have to be employed. Thus, non-vacuum, scalable, inexpensive process for single crystal semiconductors is highly desired.

It is believed that non-vacuum laser crystallization of amorphous thin film is considered as an alternative paradigm to fabricate high quality crystalline Si [1-9]. However, most of these studies rely on chemical/physical vapor deposition (CVD/PVD) or electron beam evaporation (EBE) to prepare the thin film, which inevitable increases the processing and equipment costs. Thus, a direct printing approach for Si film preparation, which can be integrated with laser crystallization, would be significant to pave the way for low cost manufacturing of high quality crystalline Si.

## 1.2. RESEARCH OBJECTIVES

The main objective of this research is to investigate laser melting and crystallization of Si in confined domains both theoretically and experimentally. Thus, five main research tasks are designed and studied carefully to achieve the objective.

(1) To systematically study the Si-$SiO_2$ interfaces in microscale using molecular dynamics (MD) simulations. The calculated interfacial energies are anticipated to favor the prediction of Si nucleation mechanism in contact with substrate (or in confined domain).

(2) Using the obtained values from MD simulations to tailor the macroscale phenomenological model. Then, the model can be applied to quantitatively

evaluate the effects of domain size and laser processing parameters on single crystal yield. Propose optimized laser processing parameters for Si crystallization.

(3) Design a proper additive manufacturing approach to prepare Si pattern. Specifically, Si nanoparticle ink will be developed for aerosol printing. The printing approach can greatly increase the productivity of Si film.

(4) Design an effective method to realize high quality crystalline Si fabrication using laser. Specifically, a pressing system is designed to densify and planarize the printed Si pattern. Meanwhile, the system is designed to prevent the heat dissipation and reduce the cooling rate.

(5) Characterize the crystalline structure of fabricated Si and establish the relationship between processing parameters and the crystallinity/morphology of manufactured Si structure. Besides, a protocol needs to be developed to use the fabricated Si.

The outcomes of above research tasks are expected to advance the fundamental understanding of laser crystallization of Si. The technical developments may benefit not only the area of laser crystallization, but also other areas, such as additive manufacturing, electronics fabrication, and coating technology.

## 1.3. ORGANIZATION OF DISSERTATION

In this dissertation, six main chapters are included. The research background and objectives are presented in Section 1, Introduction.

Then, three papers are included as the Paper section. All the three articles share a same core research topic, laser crystallization of Si, including theoretical and experimental study. Paper I focus on the interfacial energy calculation using thermodynamics integration (TI) method, which is aimed to solve task (1). Paper II emphasizes more on the macroscale model, intended to solve task (2). Based on the predictions made from paper I and II, paper III presents the experimental verification. Tasks (3) through (5) are solved one by one in this paper, where a complete new printing approach is developed to fabricate single-crystal Si.

Subsequently, conclusions are drawn for this work, mainly based on the above three papers, in Section 2.

Section 3 provides applicable recommendations for future work.

# PAPER

## I. SILICON-WALL INTERFACIAL FREE ENERGY VIA THERMODYNAMICS INTEGRATION

Wan Shou and Heng Pan

Department of Mechanical and Aerospace Engineering

Missouri University of Science and Technology, Rolla, 65401, USA.

### ABSTRACT

We compute the interfacial free energy of a silicon system in contact with flat and structured walls by molecular dynamics simulation. The thermodynamics integration method, previously applied to Lennard-Jones potentials [R. Benjamin and J. Horbach, J. Chem. Phys. 137, 044707 (2012)], has been extended and implemented in Tersoff potentials with two-body and three-body interactions taken into consideration. The thermodynamic integration scheme includes two steps. In the first step, the bulk Tersoff system is reversibly transformed to a state where it interacts with a structureless flat wall, and in a second step, the flat structureless wall is reversibly transformed into an atomistic $SiO_2$ wall. Interfacial energies for liquid silicon-wall interfaces and crystal silicon-wall interfaces have been calculated. The calculated interfacial energies have been employed to predict the nucleation mechanisms in a slab of liquid silicon confined by two walls and compared with MD simulation results.

# 1. INTRODUCTION

Manufacture of crystalline silicon wafers typically involves a directional solidification process in order to maximize grain size. In any directional solidification process, the preferred mechanism of solid silicon crystallization is continuous growth from the already-solidified region of the crystal, rather than nucleation of a new grain at the wall. The nucleation properties of the wall material become especially important when the surface area-to-volume ratio becomes large, such as in zone-melting recrystallization with encapsulating oxide/nitride layers, ribbon growth on substrate, or crystallization on dipped substrate. The interfacial interaction between silicon and the wall material can affect the nucleation behavior[1] and therefore the final grain structure. In addition, the interaction of liquid-wall will also affect the orientation of the crystal.[2] Therefore, it is desirable to understand the Si-$SiO_2$ interface in order to prevent the undesired nucleation and control the crystal orientation. This article aims at systematic studying of Si-$SiO_2$ interface in order to predict the nucleation behaviors at these interfaces.

Extensive studies have been devoted to understanding the Si-$SiO_2$ interfacial properties theoretically and experimentally. The interfacial energies concerning silicon only (liquid-crystal, crystal Si and liquid Si) have been extensively reported. The reported results on Si liquid-crystal interfacial energies are largely consistent. Apte and Zeng[3] employed cleaving wall method for the calculation of anisotropic crystal-melt interfacial free energy of silicon. The cleaving functional form is derived from the repulsive part of the two-body term of the SW potential. The calculated liquid-crystal interfacial energies are found to be in 0.34-0.42 J/$m^2$. Si liquid-crystal interfacial energies were also reported by several experimental and simulation works: 0.38 J/m$^2$ by undercooling experiment,[4] 0.4 J/m$^2$ by estimation from classical nucleation theory,[5] 0.34 J/m$^2$ from laser melting experiment,[6] 0.344-0.365 J/m$^2$ from solidification experiments,[7] 0.43 J/m$^2$ from contactless cooling experiments,[8] 0.167 J/m$^2$ using Ginzbury-Landau theory,[9] and 0.413 J/m$^2$ from MD simulation using SW and Tersoff potentials.[10] It is generally accepted that liquid-crystal interfacial energy is around 0.3-0.4 J/m$^2$. For liquid silicon interfacial energy, it has been reported to be 0.825 J/m$^2$,[11] 0.86-0.95 J/m$^2$,[12] and 0.6 J/m$^2$ from MD simulation.[13] For crystal Si, it was reported that crystal Si (111) has interfacial energy 0.59-0.83 J/m$^2$,[14] and higher values 1.23 J/m$^2$, 1.36 J/m$^2$, and 1.43 J/m$^2$ were reported for (111), (100) and (110) surfaces respectively.[15] Using the available surface energies for Si system, Li was able to conclude that nucleation of free Si slab originates from ~10-25Å below the surface.[13]

The interfacial energies between Si-SiO$_2$ interfaces (crystal Si-SiO$_2$ and liquid Si-SiO$_2$ interfaces) will be more difficult to obtain. For crystal Si-SiO$_2$, using SW-SiO potential, it is found that the interfacial energy is in the range of 1.15-1.5 J/m$^2$ between crystal silicon and SiO$_2$.[16] This is obtained from embedding nc-Si in SiO$_2$ and allowing relaxation to form SiO$_{2-x}$ suboxide layers. Kong used Monte Carlo simulation to find interfacial energies to be 0.93-1.3 J/m$^2$ for Si(001)/SiO$_2$, 1.17-1.75 J/m$^2$ for Si(110)/SiO$_2$ and 0.865-1.94 J/m$^2$ for Si(111)/SiO$_2$ depending on ionization state of Si.[17] It is found Si (111) with Si$^{+1}$ ionization state has the lowest interfacial energy. However, Tu used Monte Carlo method to identify a Si(001)-SiO$_2$ interface with lowest interfacial energy of 0.465 J/m$^2$,[18] which helps to explain commonly observed (001) orientated crystals on SiO$_2$ surfaces. For embedded nanocrystal Si in SiO$_2$, the interfacial energies are 0.8-1.6

J/m$^2$. For liquid Si-SiO$_2$ interfaces, the interfacial energy is generally estimated indirectly from contact angle. It is commonly accepted that contact angle is ~87$^o$ for a liquid Si droplet and SiO$_2$ substrate, therefore, the liquid Si-SiO$_2$ interfacial energy can be estimated indirectly using Young's equation $\gamma_{Si\text{-}SiO2} = \gamma_{SiO2} - \gamma_{Si}\cos\theta$.

In order to predict the nucleation mechanism during the quenching of a liquid Si in contact with SiO$_2$ walls, one needs to understand the wetting behaviors of liquid and solid on the walls, and have access to the interfacial energies between liquid-wall ($\gamma_{lw}$), crystal-wall ($\gamma_{cw}$), and liquid-crystal ($\gamma_{lc}$). Heterogeneous nucleation (or surface nucleation) requires a crystal partially wets the wall. The macroscopic Young's equation describing a spherical crystal resting on a wall in coexistence with the liquid phase reads, $\gamma_{cw} + \gamma_{lc}\cos\theta = \gamma_{lw}$. Partial wetting of the crystal on wall corresponds to contact angle $\theta$ in the range from 0 to $\pi$, or

$$\gamma_{cw} - \gamma_{lw} < \gamma_{lc} \tag{1}$$

From the above review, there has not been a comprehensive study containing self-consistent values for $\gamma_{cw}$-$\gamma_{lw}$ and $\gamma$lc that are obtained under same simulation or experimental condition, which makes accurate evaluations of Equ.1 and understanding of nucleation mechanism difficult. Thermodynamic integration (TI) can be used to evaluate the free energy of a given system through a reversible path linking the state of the given system and a state of known free energy.[19] Heni and Löwen[20] developed a TI scheme, where a bulk hard sphere system was reversibly transformed into a system interacting with a more and more impenetrable wall, and finally a hard wall. By combining Monte Carlo (MC) simulations and TI, they were able to obtain the hard sphere liquids (and solids)/structurelss wall interfacial free energies. Later, Fortini and co-workers[21] developed the TI method using an efficient path based on penetrable potentials in exponential form, which gave higher precision in calculation of $\gamma_{\mathrm{cw}}$ and $\gamma_{\mathrm{lw}}$ for hard sphere systems. Cleavage method have been widely used in free energy measurement and calculation both in experiment[22,23] and simulation.[24] Laird and Davidchack developed a TI method by the use of "cleaving potentials", to obtain hard-sphere crystal/liquid interfacial free energies,[25] to obtain Lennard-Jones system crystal/liquid interfacial energies,[26] and to obtain $\gamma_{\mathrm{cw}}$ and $\gamma_{\mathrm{lw}}$ for hard sphere systems at coexistence.[27] Recently, Benjamin and Horbach have applied TI method using pairwise potential with a two-step approach to calculate surface energy between wall-liquid and wall-crystal,[28,29] and crystal-liquid.[30,31] Such interfacial energies have also been combined with experiments to understand and explain heterogeneous nucleation[32-34] and wetting phenomena.[35] In this article, the two-step TI method will be extended for Tersoff potential to calculate interfacial energies for Si-$SiO_2$ systems. A comprehensive study of these interfacial energies of Si system will present based on TI technique aiming at providing consistent explanation of nucleation mechanism during the solidification of liquid Si on $SiO_2$ walls.

## 2. MODEL POTENTIAL

The silicon particles are modeled using Tersoff potential,[36]

$$U = \sum_{i=1}\sum_{j>i} V^{II}{}_{i,j} + \frac{1}{2}\sum_{i=1}\sum_{j\neq i} V^{III}{}_{i,j} \tag{2}$$

with a two-body term $V^{II}{}_{i,j} = f_C(r_{ij})\, f_R(r_{ij})$ and three-body term $V^{III}{}_{i,j} = f_C(r_{ij})\, f_A(r_{ij}) b_{ij}$. The function $f_R$ represents a repulsive pair potential and $f_A$ represents an attractive potential associated with bonds, $f_C$ is a smooth cutoff function, $b_{ij}$ describes the bond order which is a decreasing function of coordination of atoms *i* and *j*, and $r_{ij}$ is distance from atom *i* to *j*. The functions $f_R$, $f_A$, $f_C$ and $b_{ij}$ take the following forms,[37]

$$f_R(r_{ij}) = A_{ij}\exp\left(-\lambda_{ij} r_{ij}\right) \tag{3}$$

$$f_A(r_{ij}) = -B_{ij}\exp\left(-\mu_{ij} r_{ij}\right) \tag{4}$$

$$f_C(r_{ij}) = \begin{cases} 1, r_{ij} < R_{ij} \\ \frac{1}{2} - \frac{1}{2}\sin\left(\frac{\pi}{2}\frac{r_{ij} - R_{ij}}{S_{ij} - R_{ij}}\right), R_{ij} < r_{ij} < S_{ij} \\ 0, r_{ij} > S_{ij} \end{cases} \tag{5}$$

$$b_{ij} = \chi_{ij}\{1 + \beta_i^{n_i}\left[\sum_{k\neq i,j} f_C(r_{ik})\,\omega_{ik}\,\mathrm{g}(\theta_{ijk})\right]^{n_i}\}^{-\frac{1}{2n_i}} \tag{6}$$

with
$$g(\theta_{ijk}) = 1 + \frac{c_i^{\,2}}{d_i^{\,2}} - \frac{c_i^{\,2}}{\left[d_i^{\,2} + (h_i - \cos\theta_{ijk})^2\right]} \tag{7}$$

where $\theta_{ijk}$ is the bond angle between bonds *ij* and *ik*. All parameters appear in Equ.(2-7) are tabulated in Table 1 to describe all the interactions.[37] Hetero-atomic interactions (Si-O) are obtained by set mixing rules,[38] i.e., $A_{ij} = (A_i A_j)^{1/2}$, $B_{ij} = (B_i B_j)^{1/2}$, $R_{ij} = (R_i R_j)^{1/2}$, $S_{ij} = (S_i S_j)^{1/2}$, while $\lambda_{ij} = \frac{1}{2}(\lambda_i + \lambda_j)$ and $\mu_{ij} = \frac{1}{2}(\mu_i + \mu_j)$. The parameter $\chi_{ij}$ in Eq. (6) is used for tuning the strength of hetero-polar bond and dealing with charge transfer between different atoms. In order to reliably simulate Si nucleation,[13] the original $R_{Si}$ and $S_{Si}$ of Tersoff potential are adopted in current work.[39]

The three-body term $V^{III}$ describes the interaction between two primary atoms *i* and *j* which involves the contribution of the third atom *k*. For the ease of description in this work, we denote the three-body function in the following abbreviated form,

$$V^{III}{}_{i,j} = V^{III}{}_{i,j}\left(\sum_{k\neq i,j} f(r_{ij}, r_{ik})\right) \tag{8}$$

Table 1. Tersoff potential based parameters for Si-O system.[37,38]

| | Si | O |
|---|---|---|
| A(eV) | $1.8308\times10^{3}$ | $1.88255\times10^{3}$ |
| B(eV) | $4.7118\times10^{2}$ | $2.18717\times10^{2}$ |
| $\boldsymbol{\lambda}$(Å$^{-1}$) | 2.4799 | 4.17108 |
| μ(Å$^{-1}$) | 1.7322 | 2.35692 |
| β | $1.1000\times10^{-6}$ | $1.1632\times10^{-7}$ |
| n | $7.8734\times10^{-1}$ | 1.04968 |
| c | $1.0039\times10^{5}$ | $6.46921\times10^{4}$ |
| d | $1.6217\times10^{1}$ | 4.11127 |
| h | $-5.9825\times10^{-1}$ | $-8.45922\times10^{-1}$ |
| R (Å) | 2.7 | 1.7 |
| S (Å) | 3.0 | 2.0 |
| $\omega_{ik}$ | 1 | 1 |
| χ | $\chi_{Si\text{-}Si}=1$<br>$\chi_{Si\text{-}O}=1.17945$ | $\chi_{O\text{-}O}=1$<br>$\chi_{O\text{-}Si}=1.17945$ |

The TI scheme adopted in this work follows the previous reported method[28] and consists of two steps. First, a bulk Si system (Tersoff) with periodic boundary condition is transformed into an intermediate state where Tersoff system interacts with structureless flat walls. Then, in the second step, the flat walls are reversibly transformed into $SiO_2$

walls. The structureless flat wall (fw) is a purely repulsive potential interacting along the z direction and is described by the Weeks-Chandler-Anderson (WCA) potential,[28]

$$u_{flatwall}(z_i)=\begin{cases}4\varepsilon\left[\left(\dfrac{\sigma}{z_i}\right)^{12}-\left(\dfrac{\sigma}{z_i}\right)^{6}+\dfrac{1}{4}\right]\times w(z_i),\ 0<z_i\le z_{cw}\\ 0,\ z_i>z_{cw}\end{cases}\tag{9}$$

with $\varepsilon = 1.0$ eV, $\sigma = 1.7$ Å, the cut-off $z_{cw} = 2^{1/6}\sigma$, and $z_i$ is the distance of particle $i$ to one of the flat walls. The function $w(z_i)$ ensures that $u_{fw}(z_i)$ goes smoothly to zero at $z = z_{cw}$ and is given by,

$$w(z_i)=\frac{1}{1+h^4/(z_i-z_{cw})^4}\tag{10}$$

where the dimensionless parameter $h$ is set to 0.005.

## 3. CALCULATION OF INTERFACIAL FREE ENERGIES

### 3.1. HAMILTONIAN, PARTITION FUNCTIONS AND GIBBS FREE ENERGY

The Hamiltonian of the Tersoff system interacting with a wall, can be written as,

$$H(r,p)=\sum_{i=1}^{Np}\frac{1}{2m_i}p_i^{\,2}+\sum_{i=1}^{Np}\sum_{j>i}^{Np}V^{II}{}_{i,j}+\frac{1}{2}\sum_{i=1}^{Np}\sum_{j\neq i}^{Np}V^{III}{}_{i,j}\left(\sum_{k\neq i,j}^{Np}f(r_{ij},r_{ik})\right)+U_{wall}\tag{11}$$

where $p_i$ is the momentum of atom $i$, $m_i$ is the mass of atom $i$, $Np$ is the total number of Si atoms and $U_{wall}$ is the wall-atom potential. $U_{wall}$ has different forms for flat wall and $SiO_2$ walls, which are denoted as $U_{flatwall}$ and $U_{sio2wall}$ respectively. The simulation is performed in the $NP_NAT$ ensemble, where the number of particle $N$, surface area $A$, and temperature $T$ are kept constant and the length of the simulation box along the z direction is allowed to fluctuate in order to maintain a constant normal pressure $P_N$. The isothermal-isobaric partition function corresponding the Hamiltonian (11) is:[28]

$$Q_{NP_NAT} = \frac{1}{h^{3N}N!}\iiint \exp\left[-\frac{H(r,p)+P_N AL_z}{k_B T}\right] AdL_z dr^N dp^N \tag{12}$$

where *r* and *p* denote the position and momentum of the particles, *h* is the Planck constant and $L_z$ is the length of the simulation domain in *z* direction. The Gibbs free energy *G* of the system is related to the partition function (12) by

$$G = -k_B T \ln Q_{NP_NAT} \tag{13}$$

Direct calculation of Gibbs free energy using Equ.12-13 is very difficult. Instead, the following TI approach is taken. To apply TI method, parametrization with λ will be performed.

### 3.2. PARAMETRIZATION WITH Λ AND INTERFACIAL ENERGY CALCULATED BY TI

For interaction with a flat wall, the $U_{wall}$ in Equ.11 can be written as,

$$U_{flatwall} = \sum_{i=1}^{Np} u_{flatwall}(z_i) \tag{14}$$

with the following parametrization of the wall potential with λ,

$$u_{flatwall}(z_i,\lambda) = \lambda^2 4\varepsilon\left[\left(\frac{\sigma}{z_i+(1-\lambda)z_{cw}}\right)^{12} - \left(\frac{\sigma}{z_i+(1-\lambda)z_{cw}}\right)^{6} + \frac{1}{4}\right]\times w(z_i) \tag{15}$$

At $\lambda=0$, the Tersoff system can freely cross the boundaries. As $\lambda$ increases, the wall becomes more and more impenetrable and finally an impenetrable WCA wall is obtained with $\lambda=1$. The transformation from periodic boundaries to flat walls is accomplished by parametrizing the wall potential as,

$$U_{wall}(\lambda) = \sum_{i=1}^{Np} u_{flatwall}(z_i,\lambda)$$

The system Hamiltonian in Equ.11 parameterized by $\lambda$ is given by

$$H(r,p,\lambda)=\sum_{i=1}^{Np}\frac{1}{2m_i}p_i{}^2+\sum_{i=1}^{Np}\sum_{j>i}^{Np}V^{II}{}_{i,j}+\frac{1}{2}\sum_{i=1}^{Np}\sum_{j\neq i}^{Np}V^{III}{}_{i,j}\left(\sum_{k\neq i,j}^{Np}f(r_{ij},r_{ik})\right)+\sum_{i}^{Np}u_{flatwall}(z_i,\lambda) \tag{16}$$

The partial derivative of *H(λ)* with respect to $\lambda$ is given by,

$$\frac{\partial H}{\partial\lambda}=\frac{\partial U_{wall}(\lambda)}{\partial\lambda}=\sum_{i}^{Np}\left\{\frac{2}{\lambda}u_{flatwwall}(z_i,\lambda)+\frac{4\varepsilon\lambda^2 z_{cw}w(z_i)}{z_i+(1-\lambda)z_{cw}}\left[12\left(\frac{\sigma}{z_i+(1-\lambda)z_{cw}}\right)^{12}-6\left(\frac{\sigma}{z_i+(1-\lambda)z_{cw}}\right)^{6}\right]\right\} \tag{17}$$

The derivative of the Gibbs free energy with respect to $\lambda$ is,

$$\frac{\partial G(\lambda)}{\partial\lambda}=-\frac{k_BT}{Q(\lambda)}\left[\frac{\partial Q(\lambda)}{\partial\lambda}\right]=\left\langle\frac{\partial H(\lambda)}{\partial\lambda}\right\rangle_{\lambda} \tag{18}$$

where the angular brackets denote the ensemble average at a particular value of $\lambda$ in the $NP_{N}AT$ ensemble.

The Gibbs free energy difference between the two initial and final states can be written as,

$$\Delta G_{iniital->final}=G(\lambda=1)-G(\lambda=0)=\int_0^1\left[\frac{\partial Q(\lambda)}{\partial\lambda}\right]d\lambda=\int_0^1\left\langle\frac{\partial H(\lambda)}{\partial\lambda}\right\rangle_{\lambda}d\lambda \tag{19}$$

The interfacial free energy of a system with walls can be defined as a Gibbs excess free energy per area,

$$\gamma=\frac{G_{system}-G_{bulk}}{A} \tag{20}$$

with $G_{system}$ and $G_{bulk}$ the Gibbs free energies of a system with walls and bulk phase of the system. By this definition, the interfacial energy of system confined by flat walls is,

$$\gamma_{si-fw}=\frac{\Delta G_{bulk->fw}}{A}\text{, with}\qquad \Delta G_{si->fw}=\int_0^1\left\langle\frac{\partial H}{\partial\lambda}\right\rangle_{\lambda}d\lambda=\int_0^1\left\langle\frac{\partial U_{wall}(\lambda)}{\partial\lambda}\right\rangle d\lambda \tag{21}$$

For $SiO_2$ walls, $U_{wall}$ in Equ.11 takes the following form,

$$U_{sio2wall} = \sum_{i=1}^{Np}\sum_{j=1}^{Nw} V^{II}{}_{i,j} + \frac{1}{2}\sum_{i=1}^{Np}\sum_{j=1}^{Nw} V^{III}{}_{i,j}\Big[\sum_{k\neq i,j}^{Np+Nw} f(r_{ij},r_{ik})\Big] + \frac{1}{2}\sum_{i=1}^{Nw}\sum_{j=1}^{Np} V^{III}{}_{i,j}\left(\sum_{k\neq i,j}^{Np+Nw} f(r_{ij},r_{ik})\right)$$

$$+\left\{\frac{1}{2}\sum_{i=1}^{Np}\sum_{j=1}^{Np} V^{III}{}_{i,j}\left(\sum_{k\neq i,j}^{Np+Nw} f(r_{ij},r_{ik})\right) - \frac{1}{2}\sum_{i=1}^{Np}\sum_{j\neq i}^{Np} V^{III}{}_{i,j}\left(\sum_{k\neq i,j}^{Np} f(r_{ij},r_{ik})\right)\right\} \qquad (22)$$

with *Nw* the total number of atoms in $SiO_2$ wall (including Si and O atoms), *Np* the total number of Si atoms in the slab, *Nw+Np* the total number of atoms. This equation is used to compute the interactions across the Si-$SiO_2$ interface. In each loop, the atom index *(i, j or k)* loops over all atoms in the group (e.g. *Np* – all silicon atoms in slab, *Nw* - all silicon and oxygen atoms in wall, and *Np+Nw* – all atoms). The first term considers all pairwise interactions (Si-Si, Si-O) across the interface. The second and third terms represent three-body interactions with the two primary atoms (*i, j*) located on different sides of the interface. Note the second and the third terms are different due to the sequence in computing the three body interactions. The fourth term represents the three-body interactions with the two primary atoms (*i, j*) located in the Si slab. This term is written in a way that only the excessive interactions due to the presence of $SiO_2$ wall are considered. There is no kinetic energy term for the wall atoms. Since the $SiO_2$ wall particles are considered to be immobile, the potential energy between wall atoms is not included in the above Hamiltonian. In this way, all pairwise and three-body interactions across the interface due to the presence of $SiO_2$ wall have been considered.

In the second step of TI scheme, the flat wall is reversibly transformed into a $SiO_2$ wall in contact with liquid silicon. During this change, the $SiO_2$ walls are positioned at the same location as the flat walls, and there is no interaction between flat and $SiO_2$ walls.

The transformation from flat walls to SiO2 walls is accomplished by parametrizing the wall potential as,

$$U_{wall}(\lambda) = \lambda^2 U_{sio2wall} + (1-\lambda)^2 U_{flatwall}$$

$$= \lambda^2 \sum_{i=1}^{Np}\sum_{j=1}^{Nw} V^{II}{}_{i,j} + \lambda^2 \frac{1}{2}\sum_{i=1}^{Np}\sum_{j=1}^{Nw} V^{III}{}_{i,j}\left(\sum_{k\neq i,j}^{Np+Nw} f(r_{ij}, r_{ik})\right) + \lambda^2 \frac{1}{2}\sum_{i=1}^{Nw}\sum_{j=1}^{Np} V^{III}{}_{i,j}\left(\sum_{k\neq i,j}^{Np+Nw} f(r_{ij}, r_{ik})\right) \quad (23)$$

Then the λ-dependent Hamiltonian during the second step of TI is

$$H(r,p,\lambda) = \sum_{i=1}^{Np}\frac{1}{2m_i}p_i{}^2 + \sum_{i=1}^{Np}\sum_{j>i}^{Np} V^{II}{}_{i,j} + \frac{1}{2}\sum_{i=1}^{Np}\sum_{j\neq i}^{Np} V^{III}{}_{i,j}\left(\sum_{k\neq i,j}^{Np} f(r_{ij}, r_{ik})\right)$$

$$+ \lambda^2 \sum_{i=1}^{Np}\sum_{j=1}^{Nw} V^{II}{}_{i,j} + \lambda^2 \frac{1}{2}\sum_{i=1}^{Np}\sum_{j=1}^{Nw} V^{III}{}_{i,j}\left(\sum_{k\neq i,j}^{Np+Nw} f(r_{ij}, r_{ik})\right) + \lambda^2 \frac{1}{2}\sum_{i=1}^{Nw}\sum_{j=1}^{Np} V^{III}{}_{i,j}\left(\sum_{k\neq i,j}^{Np+Nw} f(r_{ij}, r_{ik})\right)$$

$$+ \lambda^2 \left\{\frac{1}{2}\sum_{i=1}^{Np}\sum_{j=1}^{Np} V^{III}{}_{i,j}\left(\sum_{k\neq i,j}^{Np+Nw} f(r_{ij}, r_{ik})\right) - \frac{1}{2}\sum_{i=1}^{Np}\sum_{j\neq i}^{Np} V^{III}{}_{i,j}\left(\sum_{k\neq i,j}^{Np} f(r_{ij}, r_{ik})\right)\right\} + (1-\lambda)^2 \sum_{i}^{Np} u_{flatwall}(z,1) \quad (24)$$

The derivative of the Hamiltonian with respect to $\lambda$ is

$$\frac{\partial H}{\partial \lambda} = \frac{\partial U_{wall}(\lambda)}{\partial \lambda} = 2\lambda \sum_{i=1}^{Np}\sum_{j=1}^{Nw} V^{II}{}_{i,j} + 2\lambda \frac{1}{2}\sum_{i=1}^{Np}\sum_{j=1}^{Nw} V^{III}{}_{i,j}\left(\sum_{k\neq i,j}^{Np+Nw} f(r_{ij}, r_{ik})\right) + 2\lambda \frac{1}{2}\sum_{i=1}^{Nw}\sum_{j=1}^{Np} V^{III}{}_{i,j}\left(\sum_{k\neq i,j}^{Np+Nw} f(r_{ij}, r_{ik})\right)$$

$$+ 2\lambda \left\{\frac{1}{2}\sum_{i=1}^{Np}\sum_{j=1}^{Np} V^{III}{}_{i,j}\left(\sum_{k\neq i,j}^{Np+Nw} f(r_{ij}, r_{ik})\right) - \frac{1}{2}\sum_{i=1}^{Np}\sum_{j\neq i}^{Np} V^{III}{}_{i,j}\left(\sum_{k\neq i,j}^{Np} f(r_{ij}, r_{ik})\right)\right\} - 2(1-\lambda)\sum_{i}^{Np} u_{flatwall}(z,1) \quad (25)$$

Finally, using Equ.20, 21, and 25, the interfacial free energy of the silicon in contact with a SiO2 wall is given by

$$\gamma_{si-sio2} = \frac{\Delta G_{bulk->fw}}{A} + \frac{\Delta G_{fw->sio2}}{A} \quad (26)$$

with $\Delta G_{fw->sio2} = \int_0^1 \left\langle \frac{\partial H}{\partial \lambda} \right\rangle_{\lambda} d\lambda = \int_0^1 \left\langle \frac{\partial U_{wall}(\lambda)}{\partial \lambda} \right\rangle d\lambda$ .

On the periodic boundary, the atoms can interact across the boundary with the atoms on the far side of the simulation box. On the periodic boundary, the atoms can exit one end and re-enter the other end. During the first step of TI, the atoms near the wall can interact with the flat wall and the atoms across the periodic boundary.

## 3.3. INTERFACIAL FREE ENERGY CALCULATED BY PRESSURE ANISOTROPY

The interfacial free energy can be calculated by employing the Kirkwood and Buff method[40] if the interfacial tension equals the interfacial free energy. This holds, for the interfaces between a liquid and flat wall. Hence, we will use interfacial free energy calculated from Kirkwood and Buff method to compare with TI calculated results for liquid-flat wall interfaces. The interfacial surface tension by Kirkwood and Buff method is:

$$\gamma = \frac{1}{2}\int_0^{L_z} \langle P_N(z) - P_T(z) \rangle dz \tag{27}$$

where $P_N$ and $P_T$ are the instant local normal and lateral pressure at $z$, the bracket indicates ensemble averages, and the factor 1/2 reflects the fact that there are two free surfaces. The instant local normal pressure $P_N(z)$ and lateral pressure $P_T(z)$ are defined as[13]:

$$P_N(z) = P_{zz}(z) \tag{28}$$

$$P_T(z) = \frac{1}{2}\left[P_{xx}(z) + P_{yy}(z)\right] \tag{29}$$

and the pressure tensor components $P_{\alpha\alpha}(z)$ $(\alpha=x,y,z)$ are calculated by,

$$P_{\alpha\alpha}(z) = \frac{1}{V(z)} \sum_{i \in V(z)} S_{\alpha\alpha,i} \tag{30}$$

where *V(z)* is the volume of a sliced slab cut parallel to the surface, and the pressure tensor $P_{\alpha\alpha}(z)$ is calculated by summation of per-atom stress ($S_{\alpha\alpha,i}$) for each atom *i* within the slice volume.

The per-atom stress $S_{\alpha\alpha,i}$ for atom *i* is calculated by,[41]

$$S_{\alpha\alpha,i} = m_i v_{\alpha,i}{}^2 + \frac{1}{2}\sum_{j\neq i}^{Na}\left(r_{\alpha,i}F_{\alpha,i} + r_{\alpha,j}F_{\alpha,j}\right) + \frac{1}{3}\sum_{k\neq i,j\neq i}^{Nd}\left(r_{\alpha,i}F_{\alpha,i} + r_{\alpha,j}F_{\alpha,j} + r_{\alpha,k}F_{\alpha,k}\right) \tag{31}$$

where the first term is the kinetic energy contribution, the second term is the pairwise contribution where *j* loops over $N_a$ neighbors of atom *i*, and the third term is the three-body contribution where *j,k* loop over all $N_d$ three-body interactions atom *i;* $v_{\alpha,i}$ is the $\alpha$ components of velocity of atom *i*, $r_{\alpha,i}$ $r_{\alpha,j}$ $r_{\alpha,k}$ are the $\alpha$ components of the atom positions, and $F_{\alpha,i}$, $F_{\alpha,j}$, $F_{\alpha,k}$ are the $\alpha$ components of forces on the atoms. For atoms across the periodic boundary, the *r* vectors are unwrapped by periodic boundary so that the interacting atoms are close together.[41]

The above pressure tensor only considers interactions among silicon atoms. The additional contribution to the pressure tensor from the structureless flat walls will be taken into account by the Irving and Kirkwood (IK) method.[42] The flat walls are located at $z_b$ and $z_t$ with infinite mass,

$$P_N{}^{flatwall}(z) = \frac{1}{A}\left\langle \sum_{i=1}^{Np} F_{flatwall}\left(z_i - z_b\right)\Theta(z_i - z)\right\rangle - \frac{1}{A}\left\langle \sum_{i=1}^{N} F_{flatwall}\left(z_t - z_i\right)\Theta(z - z_i)\right\rangle \tag{32}$$

with $F_{flatwall}(z_i) = -du_{flatwall}(z_i)/dz_i$, and $\Theta$ is the Heavyside step function.

## 4. BOP COMPUTATION

The method of bond order parameters (BOP)[43] has been widely used[13,44-47] to identify crystalline atoms from amorphous/liquid atoms and was employed in this study to identify the nucleation during the quenching of a liquid slab. Specifically, local order parameter $q_3$,[13,44,47] which is sensitive to the crystalline order, was used for Si. The local structure around the atom $i$ is given by

$$\bar{q}_{lm}(i) = \frac{1}{N_b(i)} \sum_{j=1}^{N_b(i)} Y_{lm}(\theta(\vec{r}_{ij}), \emptyset(\vec{r}_{ij})) \tag{33}$$

where the sum runs over all $N_b(i)$ bonds of atom $i$, and θ and ∅ denote the azimuthal and polar angles of orientation for bond $\vec{r}_{ij}$.

By constructing a 2$l$+1 dimensional vector $\vec{q}_l = [\bar{q}_{l,-l}, \bar{q}_{l,-l+1}, \ldots, \bar{q}_{l,l}]$, we can compute local invariants

$$q_l = \frac{1}{N_b(i)} \sum_{j=1}^{N_b(i)} \frac{\vec{q}_l(i) \cdot \vec{q}_l^{\,*}(j)}{|\vec{q}_l(i)|\,|\vec{q}_l^{\,*}(j)|} \tag{34}$$

A cutoff distance of 0.293 nm was used to select the nearest neighbor[48] and a cutoff value of $q_{3c} = -0.75$ was adopted to identify crystalline atom from liquid atoms.[44]

## 5. SIMULATION DETAILS

To integrate the equation of motion, the velocity-Verlet algorithm was used with a time step is 1*fs*. The Nose-Hoover thermostat was applied. Constant pressure was applied using the scheme of Shinoda,[49] which combines the hydrostatic equations of Martyna[50] with the strain energy proposed by Parrinello.[51] Periodic boundary conditions were employed in the x y z directions for the first step of the TI method where flat wall was introduced. In the second step of TI, periodic boundary condition was only used along the x and y directions, as illustrated in Figure 1.

During the first step of TI method, flat walls were applied at the simulation boundary in z direction (LAMMPS[52] allows flat walls imposed simultaneously with periodic boundary condition). The flat walls were physically fixed at the simulation boundary positions. NPT simulation was performed as the strength of the flat wall increases during the first step of TI with the boundary position free to move. At the end of the first step TI method, the periodic boundary condition in z direction was removed. We found the removal of periodic boundary condition has negligible impact on the system energy and surface energy, as pointed out previously.[28] During the second step of

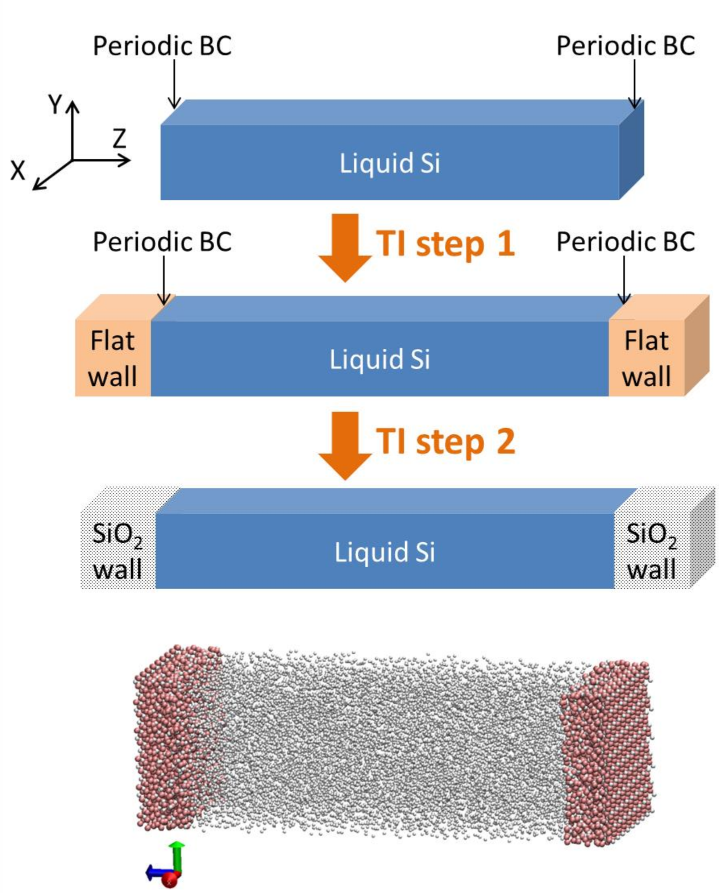

Figure 1. MD simulation configuration and the two-step thermodynamic integration scheme.

TI method, the structured walls ($SiO_2$) were introduced and fixed at the position of the flat walls. With the increase of the strength of the $SiO_2$ wall, and positions of the $SiO_2$ walls must be modified keeping the normal pressure $P_N$ constant. To ensure this, the flat wall (together with $SiO_2$ structure wall) is changed at every time step to ensure $P_N$ is constant. The individual atoms in the $SiO_2$ wall were then shifted such that they are at the same relative distance from the center of mass at the beginning of the simulation. To calculate the interfacial free energy via TI, independent simulations were performed at ~40 values of $\lambda$ between 0 and 1. The number of intervals and the interval spacing were selected to ensure a smooth profile for the thermodynamic integrand and ensure further increase of the number of intervals does not change the integration results significantly. Fewer points were used where the curve changes gradually and more dense points were placed where curve changes rapidly. At each $\lambda$, $1\times10^5$ - $2\times10^5$ timesteps were allowed to reach equilibrium before $1\times10^5$ timesteps for data averaging were performed. The data were stored every 100 timesteps and a total of 1000 configurations were collected to calculate the averaged values. Three independent runs were performed, and standard deviation was obtained from the independent runs to evaluate the variations and errors of the above described TI scheme. The trapezoidal rule was used for integration in each independent run,

$$\Delta G = \sum_{i=1}^{N_\lambda - 1} \frac{1}{2}\left[\left\langle \frac{\partial H}{\partial \lambda} \right\rangle_i + \left\langle \frac{\partial H}{\partial \lambda} \right\rangle_{i+1}\right](\lambda_{i+1} - \lambda_i) \tag{35}$$

In current study, no chemical reactions, such as oxidation or reduction, with surrounding gas will be allowed during TI process. The interaction between liquid Si and solid silicon to form gaseous compound SiO is neglected.[35,53] The $SiO_2$ substrate will be prepared before simulation and is considered fixed and immobile during the TI process. Sufficient interactions are allowed between Si-Si and Si-O atoms across the interface as described by Tersoff potential.[37] Since the interface energies will be strongly depending on bonds and interaction of un-passivated Si and O atom from $SiO_2$ substrate, we follow the following procedures to prepare $SiO_2$ substrate surface and Si solid in this study.

For $SiO_2$ surface, we did not attempt to prepare accurate reconstructions of crystalline or amorphous $SiO_2$ surface. We focus on evaluating the TI methodology to calculate interfacial energies and verify the interfacial energies by nucleation simulations. Thus, this methodology should be applicable for any arbitrary $SiO_2$ substrate. Therefore, we use an "arbitrary" approach to prepare $SiO_2$ substrates. An α-quartz crystal slab cut along (001) plane with silicon terminated surface and an area of 2500 $Å^2$ and thickness of 15Å was selected. Only the surface atoms (10Å) were allowed to relax by NPT at 1800K for $2\times10^6$ steps, and the sub-surface atoms (5Å) were fixed during the NPT relaxation. The prepared $SiO_2$ surfaces are shown in Figure 2.

For Si solid surface, we limit our focus to (111) and (001) surfaces since it has been determined the orientation on these two directions provides lowest interfacial energies (typically (110) is not the lowest). We have prepared the (001) and (111) silicon crystal surfaces with different ionization states. For flat surfaces, the ionization state of the Si atoms depends on where the Si atom are cleaved. For Si(001), the only possible state is $Si^{+2}$ as shown in Figure 2. For Si (111), there are two possibilities, $Si^{+1}$ and $Si^{+3}$. It is reported that the energy of Si(111)[$Si^{+1}$]/a-$SiO_2$ interface has the lowest interfacial energy.[17] Thus we have chosen the $Si^{+1}$ for (111) due to lowest energies reported. The selected Si crystals are shown in Figure 2.

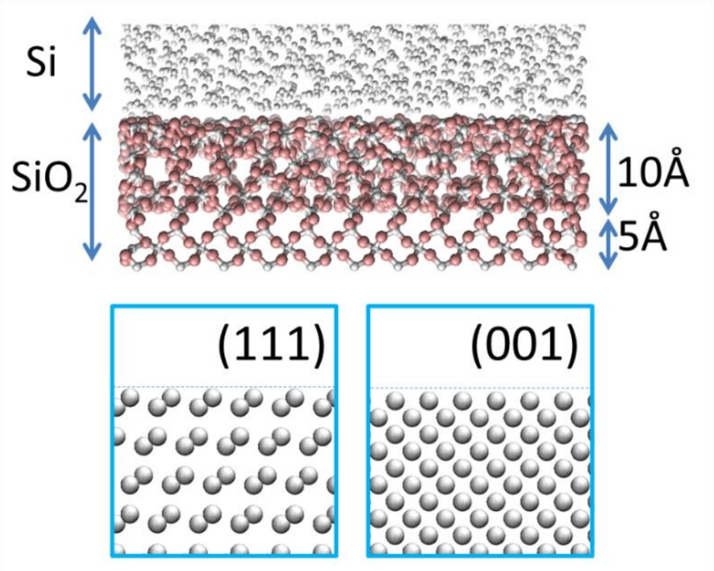

Figure. 2. The interfacial configuration between Si and SiO$_2$ (up) and selected Si crystal surfaces (down).

Table 2. The simulation dimensions for TI calculation of solid Si with confining walls.

| | X dimension (Å) | Y dimension (Å) | Z dimension (Å) | Atom number |
|---|---|---|---|---|
| (111) | 46.083 | 46.561 | 112.881 | 12495 |
| (100) | 48.879 | 48.879 | 135.775 | 16200 |

In performing simulations of crystal in contact with walls on both sides, the number of particle must be chosen such that it is compatible with the long-range order of the crystal. The simulation dimensions are chosen properly for (111) and (100) in order to maintain the long-range order. The simulation dimensions and total number of atoms in Table 2 are used. The simulations of liquid Si use the initial configuration of solid (111).

Figure 3a shows the thermodynamic integrand as a function of λ during the transformation of a bulk liquid (solid) to a confined liquid (solid) interacting with flat walls. The integrand is smooth, allowing for an accurate determination of the interfacial free energy. Figure 3b and c show the integrands as a function of λ for the second step of the thermodynamic integration when the flat wall is transformed into a structured wall. The integrand is always negative, which implies the interfacial free energy of a Si liquid (solid) in contact with a rigid structured $SiO_2$ wall is smaller than for the case where the liquid (solid) Si is in contact with a structureless flat wall.

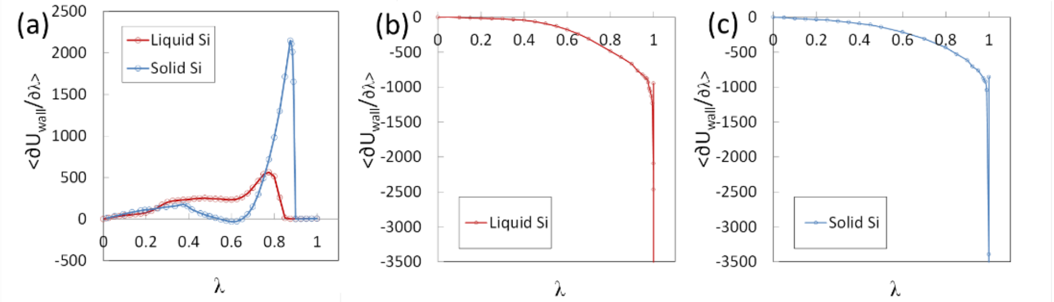

Figure 3. The thermodynamic integrand during TI steps. (a) Step 1-bulk to flat walls transition. Step 2-flat wall to $SiO_2$ wall transition for liquid Si (b) and solid Si (c).

## 6. RESULTS

### 6.1. LIQUID-FLAT WALL INTERFACIAL ENERGY

Using TI, we first determine the liquid-flat wall interfacial free energies at several temperatures and pressures, as plotted in Figure 4. The liquid-wall interfacial free energies decrease with increase in temperature. The melting point $T_m$ of Tersoff model is 2567 K,[10] which is higher than experimental value 1683 K. With $P_N = 1000$ bar, the liquid-flat wall interfacial energy calculated at 2600 K is ~0.68 J/m$^2$. This value is in reasonable agreement with 0.65 J/m$^2$ as calculated by Kirkwood-Buff method. The values from present study are slightly higher than the liquid Si-vacuum interfacial energy (0.6 J/m$^2$) reported by Li for Tersoff potential at $T=0.95T_m$.[13] It appears the introduction of confining walls increases the interfacial energy. By increasing the confining pressure to 10000 bar, the liquid-wall interfacial free energies increase to ~0.89 J/m$^2$.

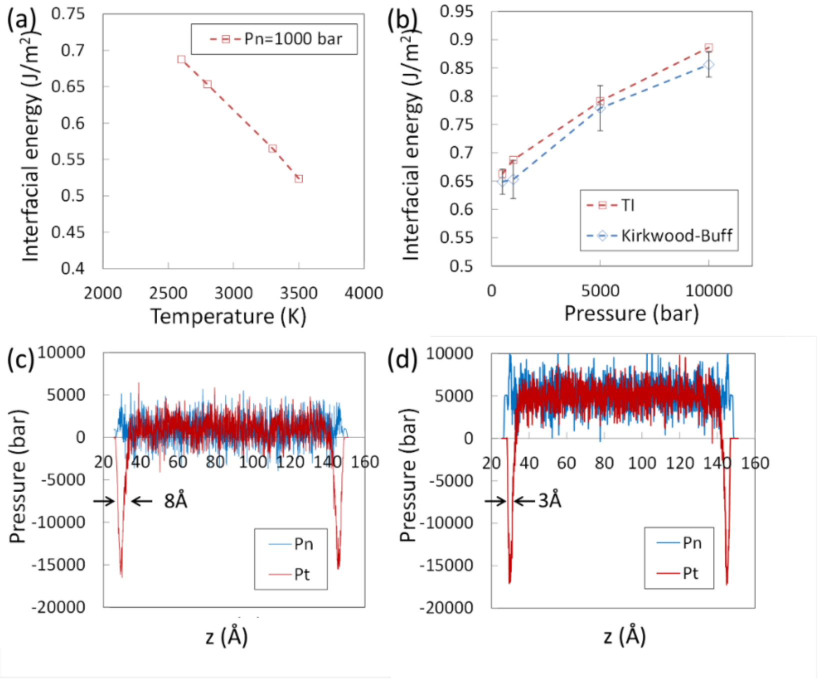

Figure 4. The interfacial energies between liquid Si and flat walls for different confining pressure (a) and temperature (b); Calculated normal and tangential pressure components under 1000 bar (c) and 5000 bar (d) confining pressures.

The difference between TI and Kirkwood-Buff calculated surface energy, as seen in Figure 4b, can be due to pressure fluctuation. Figure 4c&d shows the normal pressure and tangential pressure for two confining pressures. Large fluctuation in both normal and tangential pressure profiles in the bulk region can be seen. Since pressure calculation uses the difference between two pressure profiles, any lack of precision in the numerical measurements magnifies the relative error. The error in Kirkwood-Buff calculated surface energies are estimated from the fluctuation and included in Figure 4c&d. It should be pointed out that there is a negative pressure region near the surface. The normal confining pressure alters the width of negative pressure regions. The width decreases from 8Å to 3Å as confining pressure increases.

## 6.2. SOLID-FLAT WALL INTERFACIAL ENERGY

The solid-flat wall interfacial energies are calculated and shown in Figure 5a. We will firstly focus on close packed (111) orientation of the crystal in contact with a flat wall. In Figure 5a, we plot interfacial energy between solid Si (111) with a flat wall, as a function of temperature up to the liquid-solid coexistence temperature at $P_N$=1000 bar. For comparison, interfacial energies between liquid Si with a flat wall are also plotted in the same plot. All the interfacial energies decrease with increasing in temperature. The interfacial energies near melting temperature for liquid and solid Si in contact with flat wall are labeled as $\gamma_{lw}$ and $\gamma_{cw}$ respectively.

The values of $\gamma_{lw}$ and $\gamma_{cw}$ (the interfacial energies near melting temperature) were computed for various confining pressures and plotted in Figure 5b. It is found $\gamma_{cw}$-$\gamma_{lw}$ decreases monotonically with increasing confining pressure. With the confining pressure $P_N$=500 bar, $\gamma_{cw}$-$\gamma_{lw}$ is ~0.272 J/m$^2$. The asymptotic value of $\gamma_{cw}$-$\gamma_{lw}$, as confining pressure decrease, can be estimated to be ~0.3-0.4 J/cm$^2$. It is generally accepted that for Tersoff potential, $\gamma_{lc}$ is 0.34-0.41 J/m$^2$.[10] Thus, in a liquid Si slab weakly confined by flat walls,

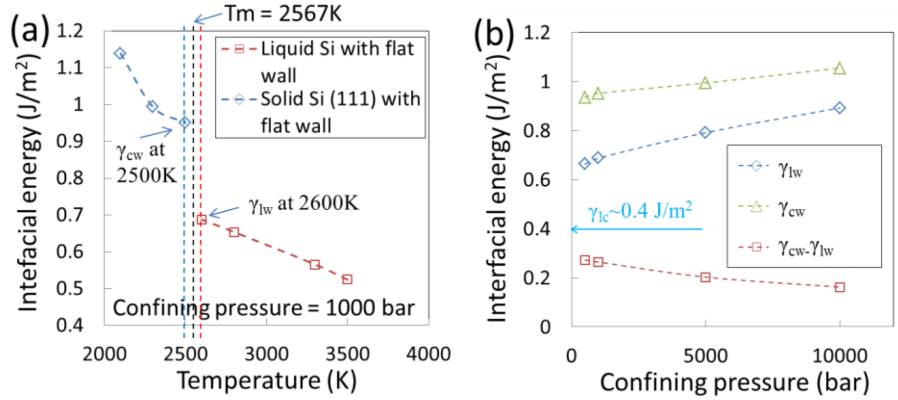

Figure 5. (a) The interfacial energies between solid Si (111) and flat walls for different temperatures; (b) The interfacial energies of liquid-wall and solid-wall near melting temperature under different confining pressures.

$\gamma_{cw}$-$\gamma_{lw}$ ~ $\gamma_{lc}$, which suggests nucleation originating from the interface (or heterogeneous nucleation) is not energetically favored. If free surface could be approximated as weakly confined slab, current result is in agreement with free surface nucleation study by Li suggesting nucleation is not originated from free surfaces.[13] In Figure 5b, it is noticed that by increasing the confining pressure, $\gamma_{cw}$-$\gamma_{lw}$ decreases from 0.272 to 0.168 J/m$^2$, which is much less than reported $\gamma_{lc}$. Thus, one can expect that the heterogeneous nucleation will occur in a slab at high confining pressure. The verification of this conclusion will be discussed in the next section.

The interfacial energy between differently orientated solid Si on flat walls were computed and plotted in Figure 6. It shows the interfaces between Si (111) and flat surface is lower than that between Si (100) and flat surface.

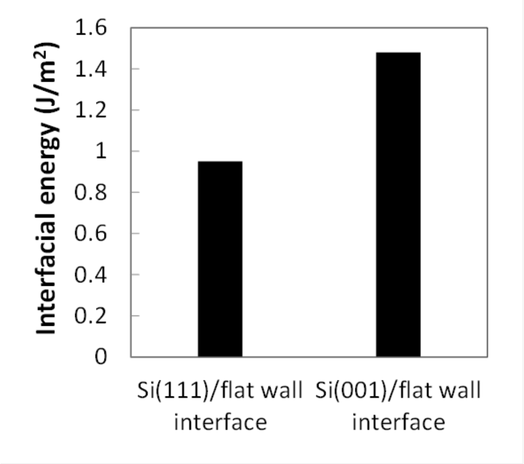

Figure 6. The interfacial energies between different orientated Si crystals with flat wall.

To test any finite-size effects, we performed additional simulations with different system sizes. It has been suggested that systems of 4000 atoms are large enough to avoid finite size effects in the calculation of interfacial free energies.[28] We calculate $\gamma_{lw}$ in larger (26250 atoms-69.12×66.515×112.881 Å$^3$) and smaller (6048 atoms-30.722×33.257×112.881 Å$^3$) systems. The computed value of $\gamma_{lw}$ increases by ~2% from the smallest system to the largest system. The increase of interfacial energy from 12495 atoms to 26250 atoms is only ~0.5%. Therefore, it is believed with system size at 12495 atoms, finite size is marginal in this work. A more systematic finite size analysis will be carried out in future work to understand the variation as system size.

### 6.3. CRYSTALLIZATION ON FLAT WALLS

In order to verify the predicted nucleation mechanism of liquid Si confined by flat walls under different confining pressures, the crystallization was monitored using the BOP method during a quenching process. The temperature was linearly ramped down from 2600K to 1000K within 5ns. There are total of 5000 samplings performed during the quenching. In each sampling, the size and location of the largest solid cluster in the liquid slab, as computed by BOP, was recorded and plotted in Figure7. Each scatter point in Figure 7 represents the location of the largest cluster during one sampling. By increasing confining pressure, more nucleation occurs at the wall surface. The preferred nucleation on the interface/surface is contributed to the lower surface energies difference $\gamma_{cw}$-$\gamma_{lw}$ as concluded from TI computation previously.

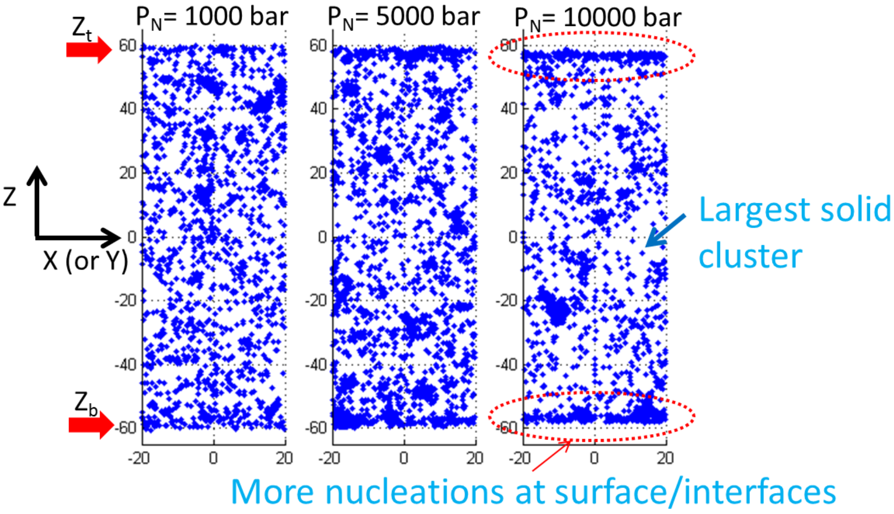

Figure 7. The distribution of nucleus in the slab under different confining pressures.

## 6.4. LIQUID SI-SIO$_2$ WALL AND SOLID SI-SIO$_2$ WALL INTERFACIAL ENERGY

The liquid-flat wall system can now be used as the reference system to calculate the interfacial free energy of the liquid in contact with a rigid SiO$_2$ wall. The external pressure is set to 1000 bar and the temperature to 2600K. The thermodynamic integrand plots are shown for liquid and solid Si on the SiO$_2$ substrates in Figure 8a and b. It is found the integrand curve shows a large kink with λ close to 1. We adopted very fine steps near λ close to 1 and performed long equilibrium runs (up to $4\times10^6$ steps). It is found significant kink appears only with λ>0.9999 (λ=0.999999), as shown in the insets of Figure 8a and b. Since the kink only occurs in a very small interval of λ, it has minor impact on the final results (i.e. removing the point at λ=0.999999 only induces <0.1% variation). Therefore, we conclude the presence of kink very close to λ = 1 has negligible effects if sufficiently fine steps are used near λ = 1. The kinks are due to extremely large value of $\sum_i^{Np} u_{flatwall}(z,1)$ (the last term in in Equ.25) when λ~1. It is believed that with λ approaching 1, the flat wall becomes very weak. Meanwhile, the atoms interact strongly with SiO$_2$ wall. Due to the atomic level un-evenness of the SiO$_2$ walls, the atoms could be very close to the perfectly flat wall, which gives rise to the large $\sum_i^{Np} u_{flatwall}(z,1)$ values. Since the term $\sum_i^{Np} u_{flatwall}(z,1)$ increases nonlinearly with (1-λ), multiplying this term with (1-λ) is not able to negate this effect. Other parameterizations could be more effective in removing the kinks and will be studied in the future work.

Using the integrand for liquid, $\gamma_{lw}$ is found to be -0.202 J/m$^2$. The negative value is due to the strong interaction between liquid Si and O atoms in the substrate. The enthalpy of formation between Si and O is -476 kJ per atom of O.[53] To understand

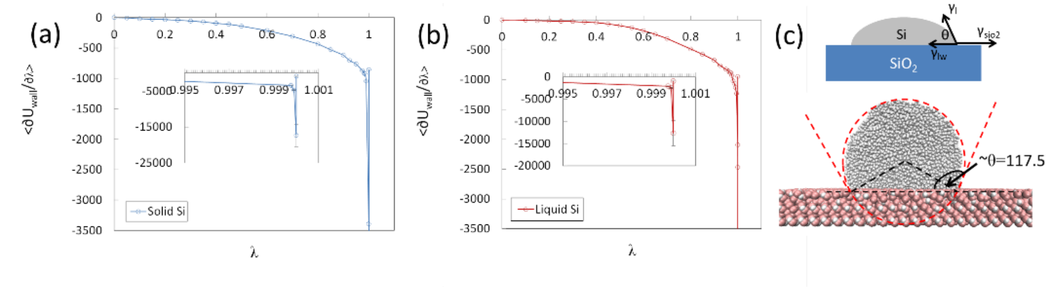

Figure 8. The thermodynamic integrand during TI step 2-flat wall to $SiO_2$ wall transition for liquid-Si (a) and solid-Si (b) interfaces; (c) Direct simulated de-wetting of liquid Si on $SiO_2$ substrate.

physical implication of the obtained $\gamma_{lw}$ value, we will consider the contact angle of a liquid Si droplet on $SiO_2$ substrate (Figure 8c). The surface energy of liquid Si ($\gamma_l$) can be estimated to be 0.68 J/m$^2$ from Figure 4a or previous results.[13] Since the solid $SiO_2$ walls are considered to be immobile in this study, it is assumed $\gamma_{sio2} = 0$. According to Young's equation $\gamma_{sio2} = \gamma_l\cos\theta + \gamma_{lw}$, it can be found the contact angle is ~72.8˚, which is in agreement with commonly accepted contact angle of a liquid Si droplet on $SiO_2$ substrates. To verify the contact angles, we perform the direct simulation of liquid Si droplet on the substrate and equilibrium contact angle was obtained after 10 ns equilibrium (Figure 8c). Similar to the reported procedure based on the contour of the droplet ,[54] we fit the outline of a liquid Si droplet using a circle, then the contact angle was defined as the angle between a tangential line of the outline through a three-phase contact point and another line on the flat surface going through the three-phase contact point. The final contact angle is averaged from 8 measurements (in the range 104-123˚) to be ~117.5˚, higher than Young's equation prediction using TI calculated values ~72.8˚. The deviation from Young's equation could be expected for nanodroplets due to the contribution of line tension effects.[55-57] The work of adhesion $W = \gamma_l(1+\cos\theta)$ can be estimated to be ~0.881 J/m$^2$ which is found to be close to experimentally measured values 0.86 J/m$^2$ for silicon on silica as measured from sessile-drop method.[43] From the contact angle and work of adhesion calculation, we conclude the arbitrarily prepared $SiO_2$ substrate is physical and can be used for crystallization study.

Using the TI integrand for solid silicon in contact with the $SiO_2$ walls (Figure 8a), $\gamma_{cw}$ is found to be 0.00691 J/m$^2$. Using the aforementioned $\gamma_{lw}$ = -0.202 J/m$^2$, it is found $\gamma_{cw}$-$\gamma_{lw}$ for Si on $SiO_2$ substrate is 0.209 J/m$^2$, slightly lower than $\gamma_{lc}$ ~0.34-0.4 J/m$^2$ as reported previously. Our TI calculation indicates weak heterogeneous nucleation will occur during the cooling of liquid Si in contact with the $SiO_2$ substrate, as will be discussed next.

## 6.5. CRYSTALLIZATION ON $SIO_2$ WALLS

The spatial distributions of the largest clusters during cooling in a slab confined by $SiO_2$ walls and an un-confined slab (free surface) are compared in Figure 9. The most prominent difference is the appearance of more large clusters (>20 atoms) in the wall confined slab. In particular, there are more large clusters found near the interface/surface region, as indicated by the red dashed circles in Figure 9b. It is also found that for wall-confined slab, clusters with atom number > 10 are absent in the region immediately (<10Å) below the interface, as indicated by the blue dashed circles. The absence of crystalline Si cluster immediately adjacent to $SiO_2$ substrate is due to the crystalline disorder introduced by $SiO_2$ surfaces. To verify this, we perform BOP analysis to identify crystalline Si (colored cyan) of a perfect Si (111) film in contact with $SiO_2$ surface. It is found a transition layer with thickness ~5-10Å can not be recognized as crystalline Si (colored white). Thus, it is suggested that compared with free surface slab, in $SiO_2$ confined slab, there are more Si clusters formed near the surface region. The interfacial energies calculated by current TI method serves the purpose to explain the enhanced nucleation near Si-$SiO_2$ interfaces.

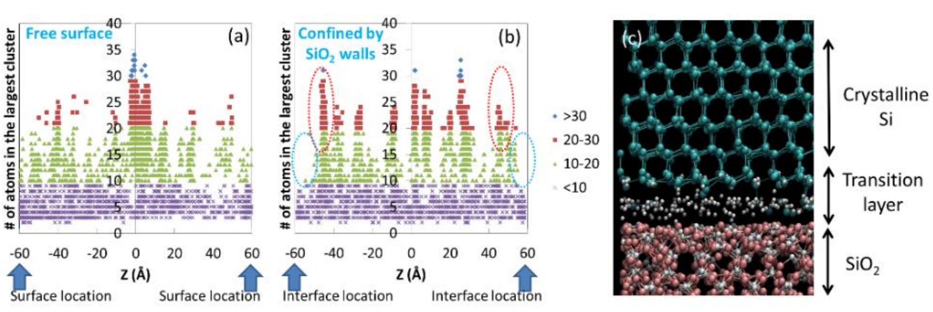

Figure 9. The location and size of the largest cluster during the cooling simulation of un-confined slab (a) and $SiO_2$ wall confined slab (b); (c) The crystalline structure at the solid Si-$SiO_2$ interface. The "crystalline" Si is colored cyan and "non-crystalline" Si is colored white.

## 7. CONCLUSION

A thermodynamics integration method to compute the interfacial free energy of a silicon system in contact with flat structureless walls and structured $SiO_2$ walls by molecular dynamics simulation is described. The method has been employed to calculate interfacial energies for liquid and solid silicon in contact with flat and structured walls. The method provides simple and reliable estimates of $\gamma_{cw}$ and $\gamma_{lw}$ that can be used with Young's equation to evaluate wettability and nucleation mechanisms. Most importantly, the method provides a general approach to calculate anisotropic crystal-wall interfacial energies for real material systems, which are hardly accessible in experiments and highly important to interpret experimental observations. The results have been used to predict and explain the observed nucleation mechanism during the quenching of a liquid Si slab confined by walls, and agreement with direct MD simulation results has been found.

## ACKNOWLEDGMENTS

This work was supported by the National Science Foundation under Grant No. 1363313. This work was also partially supported by ORAU Ralph E. Powe Junior Faculty Enhancement Award. Their financial supports are greatly appreciated.

## REFERENCES

1. T. Appapillai, C. Sachs, and E. M. Sachs, J. Appl. Phys. 109, 084916(2011).
2. K. Fujiwara, K. Maeda, H. Koizumi, J. Nozawa and S. Uda, 112, 113521(2012).
3. P. Apte and X.C. Zeng, Appl. Phys. Lett. 92, 221903(2008).
4. Y. Shao and F. Spaepen, J. Appl. Phys. 79, 2981(1996).
5. R.P. Liu, T. Volkmann and D.M. Herlach, Acta Mater. 49, 439(2001).
6. S.R. Stiffler, M.O. Thompson, and P.S. Peercy, Phys. Rev. Lett. 60, 2519(1988).
7. P.V. Evans and S.R. Stiffler, Acta Metall. Mater. 39, 2727(1991).
8. D. Li and D.M. Herlach, Europhys. Lett. 34, 423(1996).

9. X.C. Zeng and D. Stroud, J. Phys.: Condens. Matter 1, 1779(1989).
10. Y.W. Tang, J. Wang, and X. C. Zeng, J. Chem. Phys. 124, 236103(2006).
11. X. Huang, S. Togawa, S.I. Chung, K. Terashima, S. Kimura, J. Cryst. Growth 156, 52(1995).
12. Z.Q. Wang and D. Stroud, Phys. Rev. B 38, 1384(1988).
13. T. Li, D. Donadio, L. M. Ghiringhelli, and G. Galli, Nat. Mater. 8, 726(2009).
14. J. J. Métois and P. Müller, Surf. Sci. 548, 13(2004).
15. D.J. Eaglesham, A.E. White, L.C. Feldman, N. Moriya, and D.D. Jacobson, Phys. Rev. Lett. 70, 1643(1993).
16. F. Djurabekova and K. Nordlund, Phys. Rev. B 77, 115325(2008).
17. L. Kong and L. J. Lewis, Phys. Rev. B 77, 085204(2008).
18. Y. Tu and J. Tersoff, Phys. Rev. Lett. 84, 4393(2000).
19. D. Frenkel and B. Smit, *Understanding Molecular Simulation* (Academic, San Diego, 2002)
20. M. Heni and H. Löwen, Phys. Rev. E 60, 7057(1999).
21. A. Fortini and M. Dijkstra, J. Phys.: Condens. Matter, 18, L371(2006).
22. J. J. Gilman, J. Appl. Phys. 31, 2208(1960).
23. J. P. Berry, J. Appl. Phys. 34, 62(1963).
24. J. Q. Broughton and G. H. Gilmer, J. Chem. Phys. 84, 5759(1986).
25. R.L. Davidchack and B.B. Laird, Phys. Rev. Lett. 85, 4751(2000).
26. R.L. Davidchack and B.B. Laird, J. Chem. Phys. 118, 7651(2003).
27. B.B. Laird and R. L. Davidchack, J. Phys. Chem. C 111, 15952(2007).
28. R. Benjamin and J. Horbach, J. Chem. Phys. 137, 044707(2012).
29. R. Benjamin and J. Horbach, J. Chem. Phys. 139, 084705(2013).

30. R. Benjamin and J. Horbach, J. Chem. Phys. 141, 044715(2014).
31. R. Benjamin and J. Horbach, Phys. Rev. E 91, 032410(2015).
32. K. Sandomirski, S. Walta, J. Dubbert, A. Allahyarov, A. B. Schofield, H. Löwen, W. Richtering, and S. U. Egelhaaf, Eur. Phys. J.: Spec. Top. 223, 439(2014).
33. A. Reinhardt, J.P.K. Doye. J. Chem. Phys. 141, 084501(2014).
34. J. Bokeloh, G. Wilde, R. E. Rozas, R. Benjamin, and J. Horbach, Eur. Phys. J.: Spec. Top. 223, 511(2014).
35. L.D. Alphei, R. Grotjahn, C. Dobbe, M. Douvidzon, R. Janhsen, T. Gebensleben, T. Alznauer, V. Becker, J.A. Becker, J. Cryst. Growth 419, 165(2015).
36. J.Tersoff, Phys. Rev. B 39, 5566(1989).
37. S. Munetoh, T. Motooka, K. Moriguchi, and A. Shintani, Comp. Mater. Sci. 39, 334 (2007).
38. C. Y. Chuang, Q. M. Li, D. Leonhardt, S. M. Han, and T. Sinno, Surf. Sci. 609, 221 (2013).
39. B. M. Lee, T. Motooka, and S. Munetoh, J. Phys.: Condens. Matter 20, 055205 (2008).
40. J.G. Kirkwood, F.P. Buff, J. Chem.Phys. 17, 338(1949).
41. A. P. Thompson, S. J. Plimpton, and W. Mattson, J. Chem. Phys. 131, 154107 (2009).
42. J.H. Irving, J.G. Kirkwood, J. Chem. Phys. 18, 817(1950).
43. P.J. Steinhardt, D.R. Nelson, and M. Ronchetti, Phys. Rev. B 28, 784(1983).
44. T. Li, D. Donadio, G. Galli, J. Chem. Phys. 131, 224519(2009).
45. H. Pan, and C. P. Grigoropoulos, J. Appl. Phys. 115, 104307(2014).
46. H. Pan and W. Shou, J. Phys. D: Appl. Phys. 48, 225302(2015).
47. L.M. Ghiringhelli, C. Valeriani, E.J. Meijer, D. Frenkel, Phys. Rev. Lett. 99, 055702(2007).
48. S. Sastry and C.A. Angell, Nat. Mater. 2,739(2003).

49. W. Shinoda, M. Shiga, and M. Mikami, Phys. Rev. B 69, 134103(2004).

50. G.J. Martyna, D.J. Tobias and M.L. Klein, J. Chem. Phys. 101, 4177(1994).

51. M. Parrinello and A. Rahman, J. Appl. Phys. 52, 7182(1981).

52. S. Plimpton, J. Comp. Phys. 117, 1(1995).

53. R. Sangiorgi, M. L. Muolo, D. Chatain, and N. Eustathopoulos, J. Am. Ceram. Soc. 71, 742(1988).

54. R. Sangiorgi, M. L. Muolo, D. Chatain, and N. Eustathopoulos, J. Am. Ceram. Soc. 71, 742(1988); T. Werder, J. H. Walther, R. L. Jaffe, T. Halicioglu, F. Noca, and P. Koumoutsakos, Nano Lett. 1, 697 (2001); T. Koishi, K. Yasuoka, S. Fujikawa, and X. C. Zeng, ACS Nano 5, 6834 (2011); Y. Li, F. Wang, H. Liu, H. Wu, Microfluid and Nanofluid 18, 111, (2015).

55. P. G. de Gennes, Rev. Mod. Phys. 57, 827(1985).

56. T. Getta and S. Dietrich, Phys. Rev. E 57, 655(1998); L. Schimmele and S. Dietrich, Eur. Phys. J. E 30, 427(2009).

57. D. Winter, P. Virnau, and K. Binder, Phys. Rev. Lett. 103, 225703(2009); J.K. Berg, C.M. Weber, and H. Riegler, Phys. Rev. Lett. 105, 076103(2010); J. H. Weijs, A. Marchand, B. Andreotti, D. Lohse, and J. Snoeijer, Phys. Fluids 23, 022001(2011).

# II. TRANSPORT AND INTERFACIAL PHENOMENA IN NANOSCALE CONFINED LASER CRYSTALLIZATION

Wan Shou, Heng Pan

Department of Mechanical and Aerospace Engineering

Missouri University of Science and Technology, Rolla, Missouri 65409, U.S.A.

Nanomanufacturing, Laser Crystallization, Nanoscale, Confined, Surface Energies, Single crystals

## ABSTRACT

Laser processing (sintering, melting, crystallization and ablation) of nanoscale materials has been extensively employed for electronics manufacturing including both integrated circuit and emerging printable electronics. Many applications in semiconductor devices require annealing step to fabricate high quality crystalline domains on substrates that may not intrinsically promote the growth of high crystalline films. The recent emergence of FinFETs (Fin-shaped Field Effect Transistor) and 3D Integrated Circuits (3D-IC) has inspired the study of crystallization of amorphous materials in nano/micro confined domains. Using Molecular Dynamics (MD) simulation, we study the characteristics of unseeded crystallization within nano/microscale confining domains. Firstly, it is demonstrated that unseeded crystallization can yield single crystal domains facilitated by the confinement effects. A phenomenological model has been developed and tailored by MD simulations, which was applied to quantitatively evaluate the effects of domain size and processing laser pulse width on single crystal formation. Secondly, to

predict crystallization behaviors on confining walls, a thermodynamics integration scheme will be used to calculate interfacial energies of Si-SiO$_2$ interfaces.

## 1. INTRODUCTION

Many applications in semiconductor and electronic devices require the fabrication of high quality crystalline domains on substrates that may not intrinsically promote the growth of high crystalline films. Applications include thin film transistors for advanced displays [1,2], high performance thin film solar cells [3], 3D electronic devices [4], and memory devices, etc.

Various energy sources including scanning continuous wave lasers [5], electron beam sources [6], graphite strip heaters [7], and pulsed excimer lasers [8], have been utilized to crystallize amorphous materials in thin film configurations. Recently, the emergence of FinFETs (Fin-shaped Field Effect Transistor) and 3D Integrated Circuits (3D-IC) has inspired the study of crystallization of amorphous materials in nano/micro confined domains. For example, nano-graphoepitaxy is a technique that uses confining nanostructures to improve and control crystallization for monolithic 3D-IC manufacturing [9]. In FinFETs fabrication, heavy-ion bombardment of silicon fins amorphizes the surface layer of the confined fins which need to be annealed by solid phase recrystallization [10]. There have also been several efforts on confined crystallization from seeds. It is demonstrated single crystal Si can be formed by solidphase-epitaxy from Si nanowire seeds [11]. Single crystal Ge or Si can be obtained through rapid-melt-growth from Si seeds [12-14], and lateral epitaxial growth on silicon oxide from underlying seeds [15,16]. Arora et al. describe the manufacturing of single crystal confined in nanostructures by laser induced crystallization of amorphous materials on seeding substrate [17]. The seeded crystallization typically occurs in confined structures bounded by oxides or ceramics. The competition between seeded growth and heterogeneous nucleation initiated from bounding surfaces critically determines the crystallinity of final materials.

Among various confined crystallization studies, meltmediated crystallization without seeds deserves special attention. Without seeds, the crystallization relies on spontaneous nucleation which is particularly sensitive to heating/cooling conditions, surface/interfacial properties and geometrical configurations. Fundamental study of laser melting and crystallization of nano-pillars on insulating oxide was performed using in-situ TEM by Xiang [18] and In [19]. It is found without the seed, the crystallization relies on heterogeneous (or homogeneous) nucleation which is inherently difficult to control. It is unclear about the feasibility to fabricate consistent single crystal domains by unseeded crystallization from rapid melting. If feasible, which processing conditions (e.g. laser pulse width) or mechanisms could lead to single crystal formations. It is expected the size of the confinement domain is an important factor for realizing single crystal growth. This argument can be substantiated by classical nucleation theory wherein the frequency of nucleation is proportional to the volume (homogeneous) or to the interface area (heterogeneous). Furthermore, the domain size will substantially alter the temperature evaluation during the crystallization which determines the final crystallinity. Therefore, it will be desirable to develop a physics-based theoretical model coupling heat and mass transports to evaluate processing conditions as well as confinement size effects from nm to µm scales, and to guide and interpret experiments.

MD has also been applied to study confined crystallization of fins (FinFETs) and directly compared with experimental observations. MD simulation realistically captures the polycrystal region and the defect between poly-crystal and single crystal regions [10]. The confinement affects the rearrangement of the atoms near the confining surface such that the recrystallization front advances faster in the fin center than at the interfaces. This mis-match produces frequent twinning during regrowth [20]. Monte Carlo simulation also predicts the arrow tip formation and similar defect formation mechanism [21]. Recently, we performed MD simulation of the laser melting and crystallization of ZnO particles [22]. It is found that fast quenching transforms the nanoparticle from its initial hexagonal wurtzite to a cubic rock-salt structure during the recalescence stage, which could have significant implications to tailoring the performance of semiconductor nanoparticles. We also performed MD simulation of seeded crystallization in nano-confinement to reveal the confinement effects on crystallization temperatures and crystal growth dynamics [23].

In this paper, molecular dynamics simulations of laser crystallization in nano-confined domains will be presented by focusing on the following two aspects: 1. Despite the invaluable insights MD simulations provide, they are typically limited to small domain sizes (<10nm) and short times (~ns). To overcome these limitations while providing realistic descriptions at atomic level, we aim at developing a phenomenological model that can be calibrated by MD simulations. By using the developed model, we illustrate several critical features of crystallization in confined domains and demonstrate the feasibility of realizing single crystal by properly selecting laser processing and domain configurations. 2. The interfacial energies at heterogeneous interfaces are largely unknown. Thermodynamics Integration (TI) method will be used to calculate interfacial energies, which could be used to predict crystallization behaviors on confining walls.

## 2. METHOD

### 2.1. TRANSPORT IN NANO-CONFINED CRYSTALLIZATION

The classical MD simulation employing glue potential was used to model atomic interaction between Au atoms [24]. A nano-droplet (10nm in diameter, 31043 atoms) was quenched below its bulk melting temperature ($T_{eq}$=1336K) to 1200K before the rapid cooling simulations. For a rapid cooling simulation run (~6ns), the averaged computation time is ~72 hours. MD visualization is realized by VMD (Visual Molecular Dynamics).

Two types of confined droplets were simulated: freestanding droplet (bounded by free surfaces) and wall-confined droplet (bounded by confining-walls) were simulated, as illustrated in Figure 1. The wall confinement is realized by employing a structureless wall, which takes the Lennard-Jones form interacting only along the radial direction [25] with droplet atoms. The parameter of $\sigma$=0.256 nm was chosen for gold [26], the well depth $\varepsilon$ was chosen to be 0.05 eV, and $r_w - r$ is the distance between any atom and the confining wall. The confining wall is located at a distance of $r_w$ to the center of the spherical droplet. The location of the wall is allowed to move in radial direction in order to maintain a constant pressure inside droplet during simulation.

Before each rapid cooling simulation run, the undercooled nano-droplet was re-initialized by sampling atom velocities from a freshly generated Maxwell distribution at 1200K. Thus, a collection of multiple runs can effectively simulate a group of independent crystallization events. After the initialization, the droplet was coupled to the surrounding through thermal conductance G to simulate rapid quenching. Several G values were chosen: 1e6, 2e6, 3e6, 5e6, 1e7 and 5e7 W/m$^2$K and surrounding temperature $T_0$ was fixed at 800K. $T_0$ was chosen such that the substrate was temperature biased to a large fraction of the melting temperature allowing for slower cooling rates. The cooling was realized by rescaling non-translational kinetic energy of the atoms based on the heat loss rate $(T_P-T_0)\cdot G\cdot A$, where $T_P$ is averaged temperature of the droplet, and $A$ is droplet surface area in contact with surrounding. The time step is 2.8fs. For each G, 10 independent events were simulated to evaluate the probability in obtaining certain crystallinity.

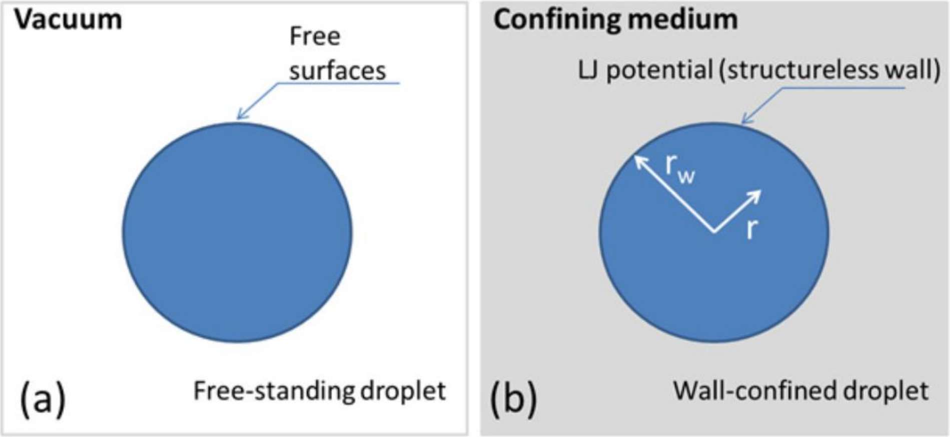

Figure. 1. Illustrations of the free-standing droplet and wall-confined droplet. The wall-confined droplet is simulated by including a Lennard-Jones potential between droplet atoms and the structureless wall.

To complement MD simulations and extend the modeling capability to large domain sizes and long time, we developed the following phenomenological model considering both heat transport and crystallization dynamics. The heterogeneous nucleation and crystal growth were modeled using a simple two-sphere model [27], with the overlapped section representing the octahedral like nucleus/crystal structure. The temperature evolution of the droplet (with the presence of crystal growth) is calculated by the energy balance equation,

$$\frac{4\pi R^3 C_v}{3v}\frac{dT_P}{dt} = \frac{\Delta H}{v}\frac{dV_s}{dt} - \frac{dE_{surface}}{dt} - (T_P - T_0)GA$$

where, $T_P$ is droplet temperature, $T_0$ is surrounding temperature, $C_v$ is the specific heat per atom, $v$ is the atomic volume ($C_v$ and $v$ are assumed to be equal between liquid and solid phases), $R$ is the radius of the droplet (or domain size), $V_s$ is the nucleus/crystal volume, $\Delta H$ is the latent heat of melting per atom, $E_{surface}$ is the excess surface energy due to the presence of the nucleus/crystal. The first two terms on right side describe the temperature change due to crystal growth, which will be zero before the detection of first nucleus.

During each Δt, it is checked if a nucleus is formed. We consider the temperature as being invariant during sufficiently small timestep Δt, and compute $\mathrm{P}^{\mathrm{NUC}}$ using the Poisson equation as:

$$P^{NUC} \cong 1 - Exp(-4\pi R^2 \cdot I \cdot \Delta t)$$

The value $P^{NUC}$ can range from zero and unity, and it physically corresponds to the probability of nucleation events during the evaluated time step. A fresh random number will be generated during each time step and compared with $P^{NUC}$. If the random number is found to be less than $P^{NUC}$ then the nucleation occurs. The surface nucleation rate I is:

$$\mathrm{I} = I_0 \exp\left(\frac{-\Delta F^*_{het}}{k_B T}\right)$$

where $I_0$ is the pre-factor $1\times10^{29}$ $\mathrm{m}^{-2}$.

Once the first nucleation occurs, the radius of nucleus/crystal $R_S$ is set to be $r^*$, which will be updated by $R_S(t+\Delta t) = R_S(t) + V_C \Delta t$, where $V_C$ is crystallization velocity:

$$V_C = c\sqrt{3k_B T/m}[1 - \exp(-\Delta\mu/k_B T)]$$

The details on the parameters used in the model can be referred to [27].

## 2.2. INTERFACIAL ENERGIES OF SI-SIO2 INTERFACES

The silicon particles are modeled using Tersoff potential [29],

$$U = \sum_{i=1}\sum_{j>i} V^{II}{}_{i,j} + \frac{1}{2}\sum_{i=1}\sum_{j\neq i} V^{III}{}_{i,j}$$

with a two-body term $V^{II}{}_{i,j} = f_C(r_{ij}) f_R(r_{ij})$ and three-body term $V^{III}{}_{i,j} = f_C(r_{ij}) f_A(r_{ij}) b_{ij}$.

The function $f_R$ represents a repulsive pair potential and $f_A$ represents an attractive

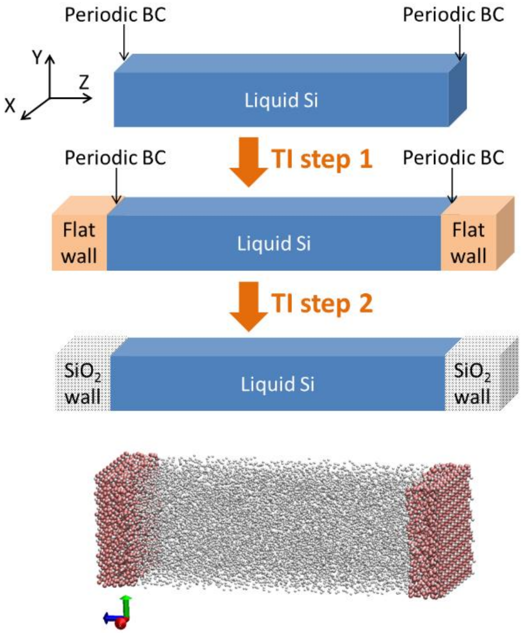

Figure 2. MD simulation configuration and the two-step thermodynamic integration scheme.

potential associated with bonds, $f_C$ is a smooth cutoff function, $b_{ij}$ describes the bond order which is a decreasing function of coordination of atoms $i$ and $j$, and $r_{ij}$ is distance from atom $i$ to $j$. The functions $f_R$, $f_A$, $f_C$ and $b_{ij}$ take the forms from [30].

The TI scheme adopted in this work follows the previous reported method [28] and consists of two steps. First, a bulk Si system (Tersoff) with periodic boundary condition is transformed into an intermediate state where Tersoff system interacts with structureless flat walls. Then, in the second step, the flat walls are reversibly transformed into $SiO_2$ walls. The structureless flat wall ($f_w$) is a purely repulsive potential interacting along the z direction and is described by the Weeks-Chandler-Anderson (WCA) potential [28].

The Hamiltonian of the Tersoff system interacting with a wall, can be written as,

$$H(r,p)=\sum_{i=1}^{Np}\frac{1}{2m_i}p_i^{\,2}+\sum_{i=1}^{Np}\sum_{j>i}^{Np}V^{II}{}_{i,j}+\frac{1}{2}\sum_{i=1}^{Np}\sum_{j\neq i}^{Np}V^{III}{}_{i,j}\left(\sum_{k\neq i,j}^{Np}f(r_{ij},r_{ik})\right)+U_{wall}$$

where $p_i$ is the momentum of atom $i$, $m_i$ is the mass of atom $i$, $Np$ is the total number of Si atoms and $U_{wall}$ is the wall-atom potential. $U_{wall}$ has different forms for flat wall and $SiO_2$ walls, which are denoted as $U_{flatwall}$ and $U_{sio2wall}$ respectively. The simulation is performed in the $NP_NAT$ ensemble, where the number of particle $N$, surface area $A$, and temperature $T$ are kept constant and the length of the simulation box along the z direction is allowed to fluctuate in order to maintain a constant normal pressure $P_N$. The isothermal-isobaric partition function corresponding the Hamiltonian is [28]:

$$Q_{NP_NAT}=\frac{1}{h^{3N}N!}\iiint\exp\left[-\frac{H(r,p)+P_NAL_z}{k_BT}\right]AdL_z dr^N dp^N$$

where $r$ and $p$ denote the position and momentum of the particles, $h$ is the Planck constant and $L_z$ is the length of the simulation domain in $z$ direction. The Gibbs free energy $G$ of the system is related to the partition function by

$$G = -k_B T \ln Q_{NP_N AT}$$

Direct calculation of Gibbs free energy using the equation is very difficult. Instead, the TI approach is used. To apply TI method, parametrization with $\lambda$ will be performed. The details of the TI method are discussed in reference [31].

## 3. RESULTS

### 3.1. TRANSPORT IN NANO-CONFINED CRYSTALLIZATION

Figure 3a-d illustrate snapshots of a single crystal growth process in a wall-confined droplet under G=1e6 W/m$^2$K. It is believed the presence of confining wall slightly reduces the excess energy to create new crystal(-wall) interfaces. As a result, more potential nucleation sites appear during the initial stage. Due to energy favorable crystal-wall interfaces, the nucleating crystals tend to grow along the periphery direction resulting in a flatter nucleating crystal (effective lower contact angle $\theta$), as can be seen in Figure 3b. As the crystallization proceeds, one large crystal can be formed while some premature nucleating crystals disappear (Figure 3c-d) which leads to single crystal formation. Comparing the temperature evolutions during crystallization between free-standing and wall confined droplets, shown in Figure 3e, the free-standing droplet exhibits lower crystallization temperatures. Interestingly, the rate of temperature rise after the onset of crystallization is higher, indicated by a steeper temperature rise, in the free-standing droplets. This suggests the difference in the liquid-solid propagation front between free-standing and wall confined droplets, as will be discussed later.

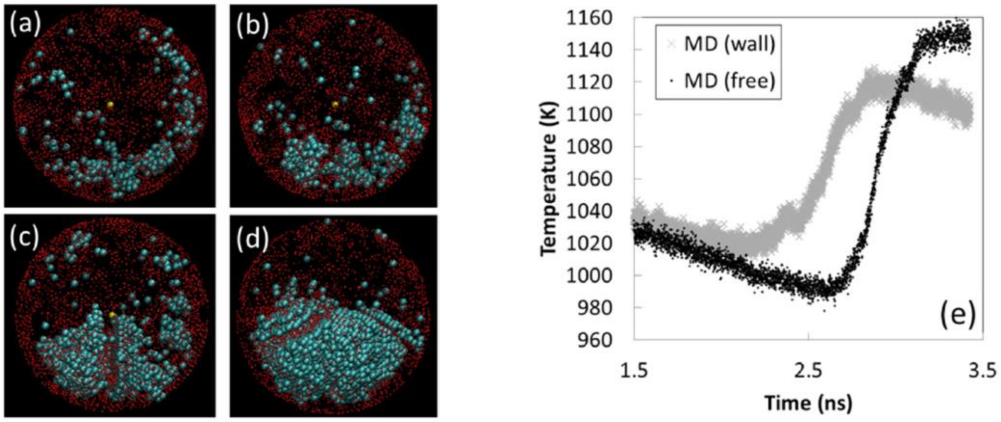

Figure 3. (a-d) Time-resolved MD snapshots to illustrate initial crystal growth in wall-confined droplets; (e) The comparison of temperature rises (as a result of latent heat release) between free-standing droplets and wall-confined droplets.

Based on above discussion, the presence of the confining wall mainly affects the morphology of the nucleating crystal and contact angle $\theta$. The contact angle $\theta$ essentially describes the interfacial energy difference between crystal-wall and liquid-wall ($\cos\theta=(\gamma_{lw}-\gamma_{sw})/\gamma_{ls}$). Based on above observation, it appears that the LJ wall interaction passivates crystal surface more than liquid surface, which would suggest a lower contact angle $\theta$ in wall-confined droplets compared with that in freestanding droplets. Therefore, we adjust the contact angle $\theta$ to simultaneously fit the crystallization temperatures in wall-confined droplet under various G values, as shown in Figure4. The results reveal with contact angle $\theta=79^\circ$ (in free-standing droplet $\theta=85^\circ$) the model predicts the crystallization temperature fairly well.

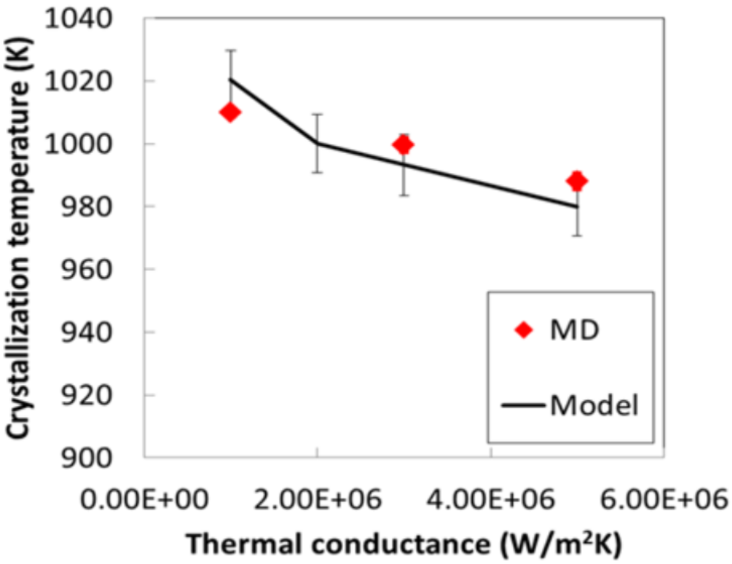

Figure 4. Validation of the phenomenogical model with MD simulation for wall-confined droplets. The comparison between MD simulated and model calculated crystallization temperature.

The developed model was then employed to calculate the probability in obtaining single crystals in 10nm wall-confined droplet. Calculated particle/droplet temperature evolutions are shown in Figure 5a along with laser profiles. The peak laser intensity is selected to ensure the particle reaches ~1400K (above melting point). As expected, long laser pulse effectively decreases the cooling rate from 2.1e9 K/s to 6.3e8 K/s for 200nm diameter droplets. Systematic studies of laser pulses width are summarized in Figure 5b-c. It is seen longer laser pulses greatly increase of the probability of forming single crystals. For domain size at 100nm or above, it is very unlikely to obtain single crystals using laser pulse width ⩽ 100ns. It has been reported in nano-graphoepitaxy experiments, it is impossible to use Excimer laser (pulse width < 100ns) to grow large grains (only grains ~10-50nm can be formed) in confining structures ~200nm. In order to

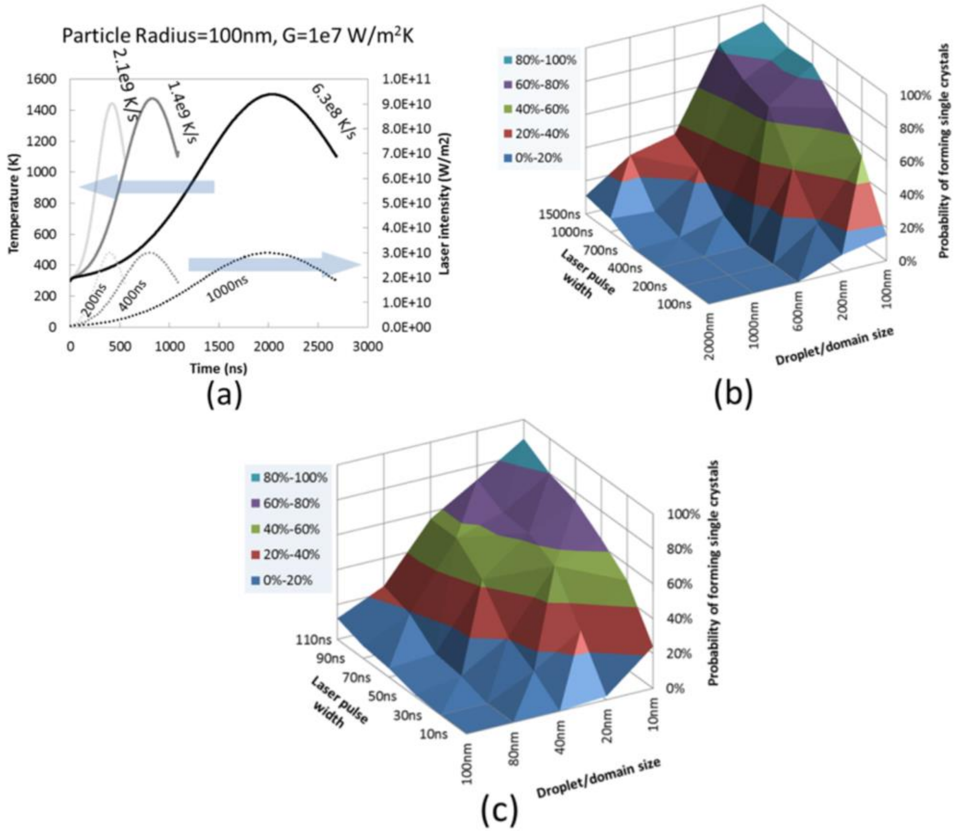

Figure 5. The predictions by the phenomenogical model to evaluate the effects of pulsed laser width on the single crystal formations. (a) Calculated temperature evolutions of the particle/droplet by various laser pulses; (b) Probability of forming single crystals in various domain sizes (⩾100nm) and laser pulse widths; (c) Probability of forming single crystals in various domain sizes (⩽100nm) and laser pulse widths.

grow ⩾ 500nm grains in confined structures, laser pulse width ⩾ μs (e.g. modulated CW Nd-YAG laser) will need to be employed, which is in agreement with our results. This seems to contradict with commonly observed large grains (up to 800nm-1000nm) obtained in pulsed laser annealing (<100ns) of thin films. It should be noted the large grain can only be observed in the central region of the laser irradiated area where heat loss is largely prevented, while at the edge much smaller grains are found. On the other hand, when domains size reduces to <100nm (e.g. FinFETs), laser pulses <100ns can be used to obtain single crystals, as illustrated in Figure 5c. Our modeling points out that laser pulse width is an important parameter for crystallization in confined structures, which should be properly selected based on domain sizes.

## 3.2. INTERFACIAL ENERGIES OF SI-SIO$_2$ INTERFACES

The thermodynamic integrand plots are shown for liquid and solid Si on the SiO$_2$ substrates in Figure 6a and b. It is found the integrand curve shows a large kink with λ close to 1. We adopted very fine steps near λ close to 1 and performed long equilibrium runs (up to $4\times10^6$ steps). Using the integrand for liquid, $\gamma_{lw}$ is found to be -0.202 J/m$^2$. The negative value is due to the strong interaction between liquid Si and O atoms in the substrate. The enthalpy of formation between Si and O is -476 kJ per atom of O. To understand physical implication of the obtained $\gamma_{lw}$ value, we will consider the contact angle of a liquid Si droplet on SiO$_2$ substrate (Figure 6c). The surface energy of liquid Si ($\gamma_l$) can be estimated to be 0.68 J/m$^2$ from previous results. Since the solid SiO$_2$ walls are considered to be immobile in this study, it is assumed $\gamma_{SiO2} = 0$. According to Young's equation $\gamma_{\text{sio2}} = \gamma_l cos\theta + \gamma_{lw}$, it can be found the contact angle is ~72.8˚, which is in agreement with commonly accepted contact angle of a liquid Si droplet on SiO$_2$ substrates. To verify the contact angles, we perform the direct simulation of liquid Si droplet on the substrate and equilibrium contact angle was obtained after 10 ns equilibrium (Figure 6c). Similar to the reported procedure based on the contour of the droplet, we fit the outline of a liquid Si droplet using a circle, then the contact angle was defined as the angle between a tangential line of the outline through a three-phase contact

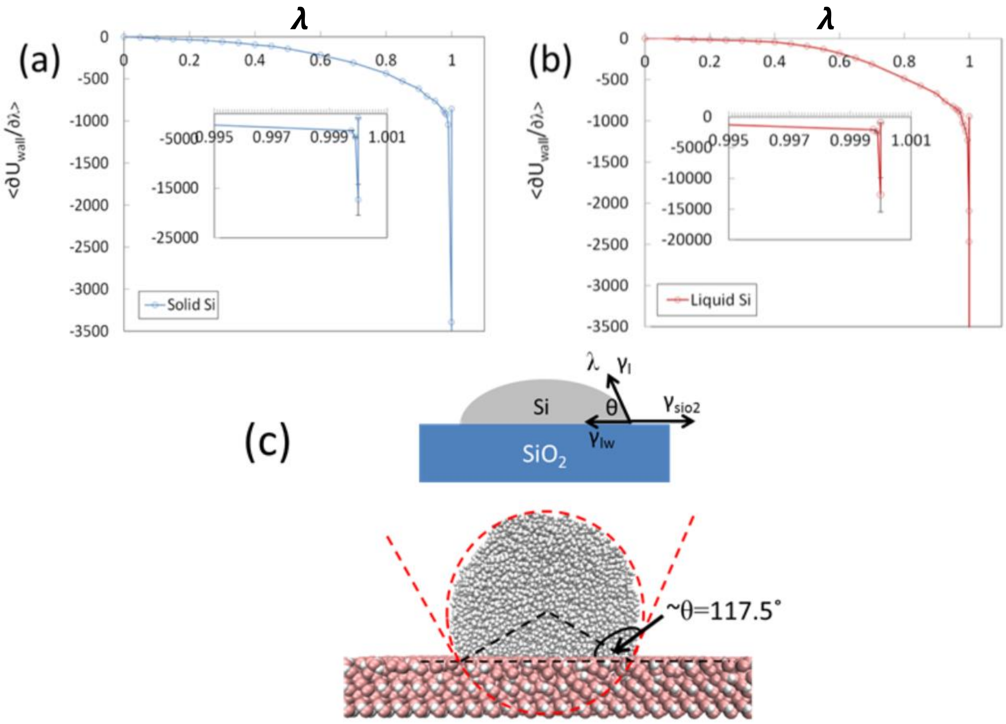

Figure 6. The thermodynamic integrand during TI step 2-flat wall to $SiO_2$ wall transition for liquid-Si (a) and solid-Si (b) interfaces; (c) Direct simulated liquid Si droplet on $SiO_2$ substrate.

point and another line on the flat surface going through the three-phase contact point. The final contact angle is averaged from 8 measurements (in the range 104-123˚) to be ~117.5˚, higher than Young's equation prediction using TI calculated values ~72.8˚. The deviation from Young's equation could be expected due to the contribution of line tension effects in nanodroplets, and the dependence of $\gamma_{lw}$ on pressure. The work of adhesion $W=\gamma_l(1+\cos\theta)$ can be estimated to be ~0.881 J/m$^2$ which is found to be close to experimentally measured values 0.86 J/m$^2$ for silicon on silica as measured from sessile-drop method. From the contact angle and work of adhesion calculation, we conclude the arbitrarily prepared $SiO_2$ substrate is physical and can be used for crystallization study.

Using the TI integrand for solid silicon in contact with the $SiO_2$ walls (Figure 6a), $\gamma_{sw}$ is found to be 0.00691 J/m$^2$. Using the aforementioned $\gamma_{lw}$= -0.202 J/m$^2$, it is found $\gamma_{sw}$-$\gamma_{lw}$ for Si on $SiO_2$ substrate is 0.209 J/m$^2$, slightly lower than $\gamma_{ls}$ ~0.34-0.4 J/m$^2$ as reported previously. Our TI calculation indicates weak heterogeneous nucleation will occur during the cooling of liquid Si in contact with the $SiO_2$ substrate.

## 4. CONCLUSIONS

In conclusion, we have performed MD simulations of unseeded crystallization in confined domain subjected to rapid cooling. A phenomenological model and methodology to tailor the model with MD simulation are described, which can be applied to extend the capability of MD simulation. Small domain size is critical to increase probability of forming single crystals. Even though small domain size induces higher cooling rate due to higher surface area to volume ratio, the probability of form single crystals still increases. Heating pulse (laser) width needs to be optimized for confined crystallization. In domain size $\geqslant$ 100nm, nanosecond laser pulse ($\leqslant$100ns) is incapable of forming single crystals in agreement with experimental observations.

A thermodynamics integration method to compute the interfacial free energy of a silicon system in contact $SiO_2$ walls by molecular dynamics simulation is described. The method provides simple and reliable estimates of $\gamma_{sw}$ and $\gamma_{lw}$ that can be used with Young’s equation to evaluate wettability and nucleation mechanisms.

## ACKNOWLEDGEMENTS

This work was supported by the National Science Foundation under Grant No. 1363313. This work was also partially supported by ORAU Ralph E. Powe Junior Faculty Enhancement Award. Their financial supports are greatly appreciated.

## REFERENCES

[1] Im J S, Kim H J 1994 On the super lateral growth phenomenon observed in excimer laser induced crystallization of thin Si films Appl. Phys. Lett. 64 2303

[2] Brotherton S D 1995 Polycrystalline silicon thin film transistors Semicond. Sci. Technolol. 10 721

[3] Andrae G, Bergmann J, Falk F, Ose E 1999 In-situ diagnostics for preparation of laser crystallized silicon films on glass for solar cells Thin solid films 337 98

[4] Ishihara R, Derakhshandeh J, Mofrad M R T, Chen T, Golshani N, Beenakker C I M 2012 Monolithic 3D-IC with single grain Si thin film transistors Solid-state electronics 71 80-87

[5] Buchner R, Haberger K, Seitz S, Weber J, Seegebrecht P 1990 3D COMS devices in recrystallized silicon Microelectronics Journal 21(6) 13-20

[6] McMahon R A 1988 Formation of silicon-on-insulator layers by electron beam recrystallization Microelectronic Engineering 8 255-272

[7] Geis M W, Antoniadis D A, Silversmith D J, Mountain R W, Smith H I 1980 Silicon graphoepitaxy using a strip-heater oven Appl. Phys. Lett. 37 454

[8] Kumomi H 2003 Location control of crystal grains in excimer laser crystallization of silicon thin films Appl. Phys. Lett. 83 434

[9] Crnogorac F, Witte D J, Xia Q, Rajendran B, Pickard D S, Liu Z, Mehta A, Sharma S, Yasseri A, Kamins T I, Chou S Y, Pease R F W, 2007 Nano-graphoepitaxy of semiconductors in 3D integration Micorelectronic Engineering 84 891-894

[10] Lampin E, Krzeminski 2011 Regrowth of oxide-embedded amorphous silicon studied with molecular dynamics J. Appl. Phys. 109.123509

[11] Woo Y S, Kang K, Jo M, Jeon J, Kim M 2007 Solid-phase epitaxy of amorphous Si using single-crystalline Si nanowire seed templates Appl. Phys. Lett. 91 223107

[12] Liu Y, Deal M D, Plummer J D 2004 High-quality single-crystal Ge on sinsulator by liquid-phase epitaxy on Si substrates Appl. Phys. Lett. 84 2563

[13] Miyao M, Toko K, Tanaka T, Sadoh T 2009 High-quality single crystal Ge stripes on quartz substrate by rapid-melt-grwoth Appl. Phys. Lett. 95 022115

[14] Toko K, Sakane T, Tanaka T, Sadoh T, Miyao M 2009 Defect-free single-crystal Ge island arrays on insulator by rapid-melting-growth combined with seed positioning technique Appl. Phys. Lett. 95 112107

[15] Cammilleri V D, Yam V, Fossard F, Renard C, Bouchier D, Fazzini P F, Hytch M 2009 Growth kinetics of Ge crystals on silicon oxide by nanoscale silicon seed induced lateral epitaxy J. Appl. Phys. 106 093512

[16] Matsumura R, Tojo Y, Kurosawa M, Sadoh T, Mizushima I, Miyao M 2012 Growth-rate-dependent laterally graded SiGe profiles on insulator by cooling-rate controlled rapid-melting-growth Appl. Phys. Lett. 101 241904

[17] Arora H, Du P, Tan K W, Hyun J K, Grazul J, Xin H L, Muller D A, Thompson M O, Wiesner U 2010 Block copolymer self-assembly directed single-crystal home and heteroepitaxial nanostructures. Science 330 214-219

[18] Xiang B, Hwang D J, In J B, Ryu S G, Yoo J H, Dubon O, Minor A M, Grigoropoulos C 2012 In Situ TEM near-field optical probing of nanoscale silicon crystallization Nano Lett. 12 2524

[19] In J B, Xiang B, Hwang D J, Ryu S, Kim E, Yoo J, Dubon O, Minor A M, Grigoropoulos C 2014 Generation of single crystalline domain in anno-scale silicon pillars by near-field short pulsed laser Applied Physics A 114 277-285

[20] Marques L A, Pelaz L, Santos I, Lopez P, Duffy R 2012 Molecular dynamics simulation of the regrowth of nanometric multigate Si devices J. Appl. Phys. 111 034302

[21] Martin-Bragado I, Moroz V 2009 Facet formation during solid phase epitaxy regrowth: A lattice kinetic Monte Carlo model Appl. Phys. Lett. 95 123123

[22] Hu M, Poulikakos D, Grigoropoulos C, Pan H 2010 Recrystallization of picosecond laser-melt ZnO nanoparticles in a liquid: a molecular dynamics study J. Chem. Phys. 132 164504

[23] Pan H, Grigoropoulos C 2014 Crystallization in nanoconfinement seeded by a nanocrystal-a molecular dynamics study J. Applied Physics 115 104307

[24] Ercolessi F, Parrinello M, Tosatti E 1988 Simulaiton of gold in the glue model Philosophical Magazine A 58 213

[25] Benjamin R, Horbach J 2013 Lennard-Jones systems near solid walls: computing interfacial free energies from molecular simulation method J. Chem. Phys. 139 084705

[26] Agrawal P, Rice B M, Thompson D L 2002 Predicting trends in rate parameters for self-diffusion on FCC metal surfaces. Surface Science 515 21-35

[27] Pan H, Shou W 2015 Single crystal formation in micro/nanoconfined domains by melt-mediated crystallization without seeds J. of Phys. D: Appl. Phys 48 (22)

[28] R. Benjamin and J. Horbach, 2012 Wall-liquid and wall-crystal interfacial free energies via thermodynamic integration: A molecular dynamics simulation study. J. Chem. Phys. 137, 044707.

[29] J.Tersoff, 1989 Modeling solid-state chemistry: Interatomic potentials for multicomponent systems. Phys. Rev. B 39, 5566.

[30] S. Munetoh, T. Motooka, K. Moriguchi, and A. Shintani, 2007 Interatomic potential for Si-O systems using Tersoff parameterization. Comp. Mater. Sci. 39, 334

[31] Shou W, Pan H 2016 Silicon-wall Interfacial Free Energies via Thermodynamics Integration J. Chem. Phys. 145(18), 184702.

# III. DIRECT PRINTING SINGLE-CRYSTAL SI ISLANDS BY MICROSCALE NANOPARTICLE PRINTING AND CONFINED LASER MELTING AND CRYSTALLIZATION

## ABSTRACT

Non-vacuum printing process has been demonstrated for a large variety of organic and inorganic materials. Currently, the printed films are dominantly in amorphous, polycrystalline or nanoparticle films. Printing single-crystal semiconductor structures is highly important to enhance the performance of printable electronics. In this article, manufacturing of single-crystal silicon micro/nano islands is demonstrated. Silicon nanoparticle ink was aerosol printed followed by confined laser melting and crystallization allowing manufacturing of single-crystal silicon micro/nano islands. It is also shown as-fabricated Si islands can be transfer printed onto flexible polymer substrates for heterogeneous integration of organic-inorganic materials. The additive nature of this technique suggests a scalable and economical approach for high crystallinity semiconductor printing.

Aerosol printing, laser crystallization, confinement, silicon nanoparticle ink, flexible electronics

## 1. INTRODUCTION

Direct printing, as a large area and low-cost fabrication technology, has received increasing interest and become essential for the development of flexible/stretchable electronics[1-4], and emerging microelectronics[5-6]. Various conductive materials, such as metal nanoparticles/nanowires[7-10], carbon nanotube[11-13], graphene[14,15], and so on, have been printed for electrodes and antenna, etc. As key components in electronics, both organic[16-18] and inorganic[19-22] semiconductors have also been printed for various applications such as diodes and transistors. Single-crystals are highly desired for high performance device fabrication due to their high mobility[23]. Recently, printing single-crystal organic semiconductor[24-27] and organic-inorganic hybrid perovskites[28,29] have been demonstrated. Meanwhile, direct printing of single crystal inorganic semiconductor (such as Si and Ge) has posed significant technical challenges. Among them, printing single-crystal nanowires appears the most promising although controlling location and orientation of nanowire array in a large area is still an active area of research[30-32]. By now, inorganic single-crystal semiconductor device fabrication mainly relies on lithographic processing[33,34], and vacuum based vapor-liquid-solid growth approaches[35,36]. Thus, non-vacuum, scalable, inexpensive process for single-crystal semiconductors manufacturing is highly desired.

Single-crystal Si is still the most widely used semiconductor in electronic and optoelectronic applications, such as high-performance transistors[37,38], photovoltaics[39,40] and photodetector[41], etc. However, single-crystal Si manufacture largely relies on Czochralski (Cz) growth method[42]. As-fabricated Si wafers have recently been used to fabricate micro/nano silicon ribbons for high performance flexible electronics[30-32]. Non-vacuum crystallization of amorphous thin film is considered as an alternative paradigm to fabricate high quality crystalline Si[43]. Various energy sources have been utilized to crystallize amorphous Si thin film, including pulsed and continuous wave (CW) lasers[37,44-50], electron beam[51], and strip heater[52]. In order to directly crystallize a-Si film to single-crystal on amorphous substrates, such as $SiO_2$, it would be preferred that all the materials are melted to exclude any pre-existed nucleus[53]; thereby, lead to a scenario where crystal growth from limited nucleation sites (ideally one nucleation site), which maximizes the crystalline grain size[54]. Typically, sizes of the islands are several tens of µm in length and width, and <1 µm in thickness. Such sizes are sufficiently large for preparation of many devices and sufficient small to ensure single crystalline growth of the islands. Gibbons[55] shows 20 µm×2 µm Si islands on amorphous substrate can be laser recrystallized with formation of single-crystalline stripes. Nanoscale single-crystal fabrication[44,56,57] has been demonstrated recently. It has been demonstrated that single crystal can be generated in confined domains on amorphous substrates both theoretically[58] and experimentally[53,56,59]. The size should be correlated with the sizes of laser beams as well as the pulse duration (scanning speed) used for recrystallization in order to increase the probability of forming single crystal[58]. From previous literatures, three typical confining configurations are used: (1) Using pre-patterning techniques to confine the Si within a well-defined domain[49,60], rather than a whole film; (2) Confining Si within a capillary[41,61] or isolating Si as a nanopillar[53,56,59]; and (3) embedding or capping Si with silicon oxide layer[62,63], which also depress the dewetting[64-67]. Generally, confinement provides an effective way to prevent heat dissipation, modulate cooling rate and prevent dewetting of melted thin films. However, a straightforward and reusable confining method is needed to simplify the process and lower the cost. Most of these studies rely on vacuum-based chemical/physical vapor deposition (CVD/PVD) or electron beam evaporation (EBE) to prepare the thin film, which inevitably increases the processing and equipment costs.

Laser crystallization is an excellent candidate due to its versatility such as vacuum-free/maskless nature, area-selective rapid processing, and scalability to large-area manufacturing. The robust crystallization method for large area processing can be combined with a direct printing approach for Si film preparation, which is becoming significant for low cost manufacturing of high performance devices[68-72]. Here, we reported a facile manufacturing scheme for printing single-crystal Si islands in ambient environment. An industrial viable microscale printing approach, i.e. aerosol printing, is used to print silicon nanoparticle (NP) patterns on wafer scales. Subsequently, a quartz slide was employed to densify and planarize the printed Si nanoparticle films. By scanning a CW laser through the quartz piece, which worked as a removable confinement surface, the Si nanoparticles sandwiched between the quartz and substrate can be melted and crystallized. The laser melted liquid stripe could break into separated islands, whose size, spacing and morphology can be dictated by laser scan speed and confining gaps (the packing density of the nanoparticles). The isolated domains are in microscale range which contain limited number of nucleation sites facilitating single crystal formation. The confining surface (e.g. quartz) is removed after laser crystallization. To prevent or reduce the attachment of crystalized structures on quartz, the substrate (e.g. nitride) exhibiting higher adhesion with Si compared with quartz could be used. The entire process circumvents expensive equipment (such as CVD or PVD, and photolithography), while maintaining high quality of crystallized Si, which paves the way toward low-cost high-performance device fabrication.

## 2. RESULTS AND DISCUSSION

Figure 1 (a) illustrates the single-crystal Si ribbon printing process that can be directly integrated with flexible substrates. Si patterns were firstly prepared by aerosol printing on Si substrates with 2 µm oxide or nitride films. The aerosol printing generates linewidth down to ~20 µm, as shown in Figure1b-i. Printed linewidth is mainly controlled by adjusting printing speed (1-5mm/s, details in Figure S1). The Si ink preparation and printing process are described in Methods. Ribbons with a tapered tip containing features down to ~10 µm can also be printed. A photograph of printed Si patterns on wafer scales is displayed in Figure 1b-ii, which was printed within minutes.

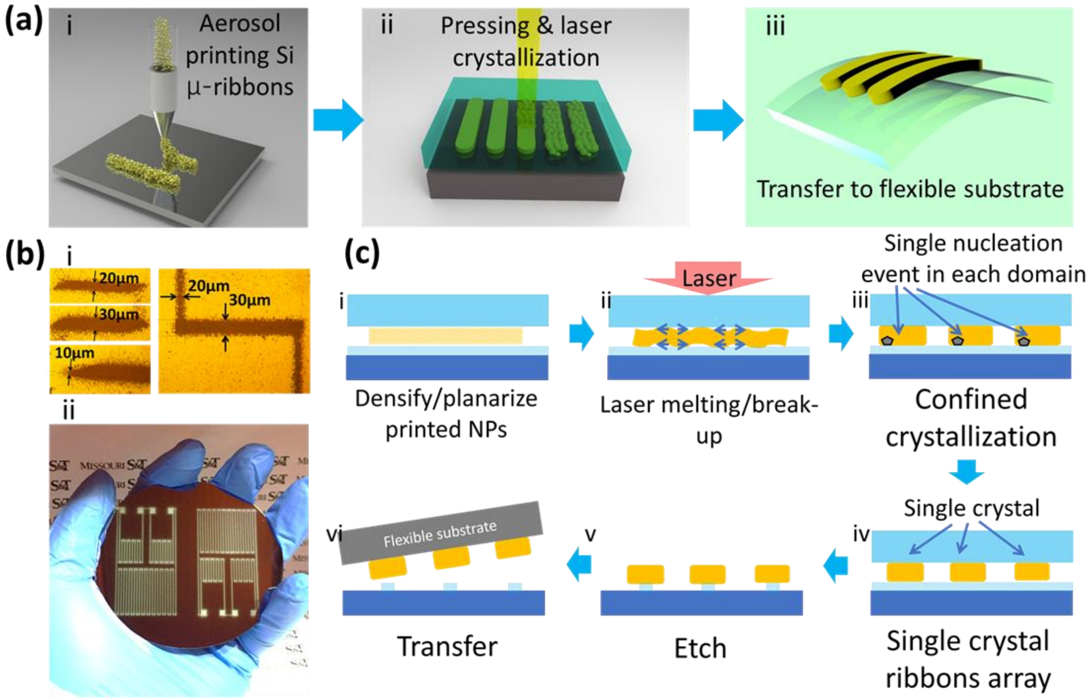

Figure 1. (a) Conceptual design of laser direct writing of crystalline nano-ribbon in confinement: i. Aerosol printing of microscale pattern using Si NPs; ii. Pressing and confined laser crystallization; iii. Transfer print of fabricated Si to flexible substrate; (b) Representative photographs of printed Si pattern: i. The smallest continuous line; ii. Wafer scale printing; (c) Detailed procedures for single-crystal Si ribbon manufacturing: (i) Densify/planarize of printed Si NPs; (ii) Laser melting/break-up of printed NPs; (iii)(iv) Single crystal nucleation and growth; (v) Disassembly and etching of single-crystal ribbons array; (vi) Transfer of crystalline Si ribbon to flexible substrate.

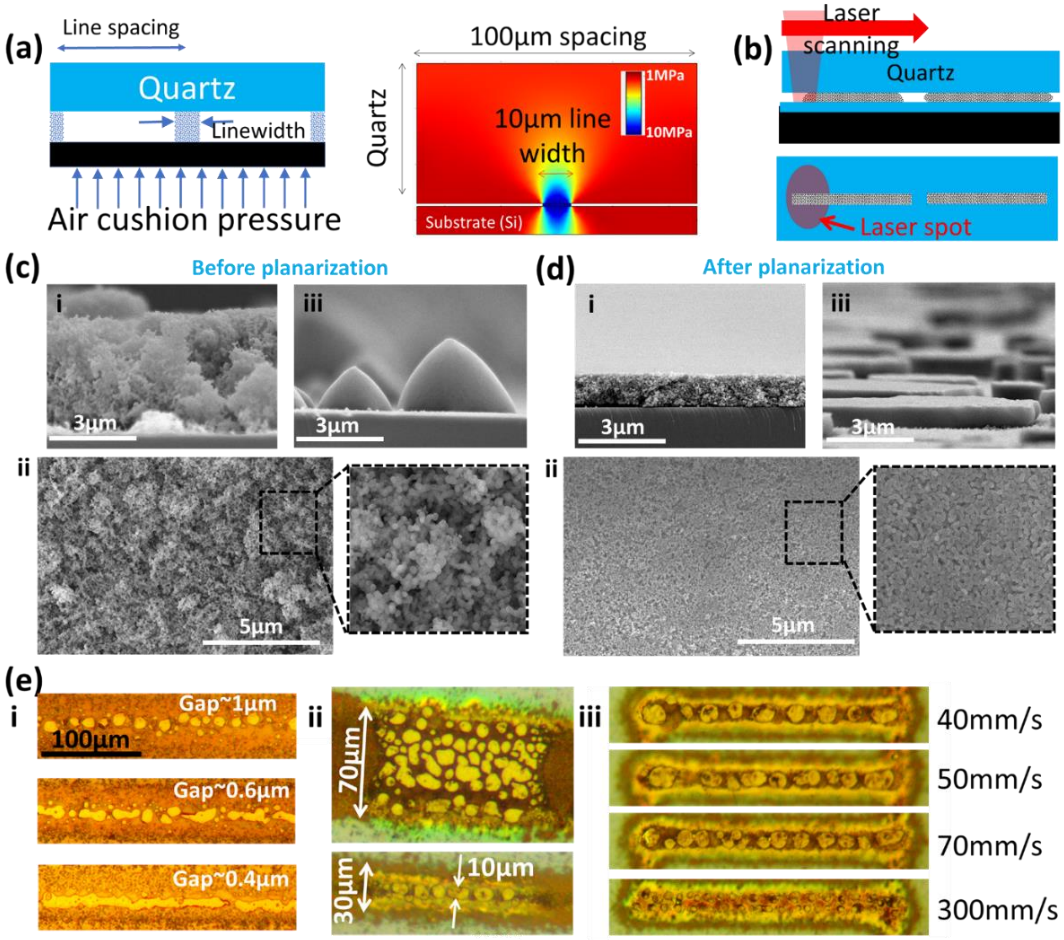

Figure 2. The influence of pressing-assisted confining on sintering of Si nanoparticles. (a) Schematic of pressing and corresponding FEM simulation. (b) Schematic of confined laser processing (side view and top view) (c) Printed Si nanoparticle without pressing (i) Cross-section SEM image of the as printed Si NPs. (ii) Top view SEM image of the printed Si NPs (low and high magnifications) (iii) Si dewets after sintering without confinement. (d) Printed Si nanoparticle after pressing (i) Cross-section SEM image of the pressed Si NPs. (ii) Top view SEM image of the pressed Si NPs (low and high magnifications) (iii) Flat Si domains after sintering with confinement. (e) Optical images of Si NPs processed with different parameters: (i) gap, (ii) linewidth, and (iii) scanning speed.

The printed Si patterns exhibiting high porosity and rough surfaces were then pressed and planarized using a transparent quartz slide (fused silica, details can be found in Materials and Methods), as indicated in Figure 1c-i. To ensure uniform pressing and confinement over a large area, air cushion pressing used in nanoimprinting process is utilized[73]. An inflatable airbag was incorporated in the system with pressure supplied and regulated by a gas cylinder. The details of the pressing system are described in supplementary materials (Figure S2). CW laser irradiates through the quartz slide on the planarized and confined Si patterns to induce melting and recrystallization (as illustrated in Figure 1a-ii and 1c-ii-iv). The laser scanning speed from 30 mm/s to 300 mm/s were tested. After disassembling, the crystallized Si can be peeled off (Figure 1c-v&vi) and transferred to the target polymer substrates (Figure 1a-iii).

Pressure up to 2.5 MPa has been reported[73] for nanoimprinting by air cushion. Finite element method (FEM) simulation (Figure 2a) shows that with 1 MPa air cushion pressure, the pressure applied on aerosol printed lines can reach 10 MPa (assuming 100 µm line spacing and 10 µm linewidth). It is reported that nanopowders can be dry pressed and cold-welded to green density (>62%) by 50 MPa uniaxial pressure[74-76]. Thus, it is believed nanoparticle packing density >50% can be achieved with ~1 MPa air cushion pressing. The pressure in the range of 0.68-0.83 MPa are used in current study. Planarization and densification of printed nanoparticles can be clearly observed in the scanning electron microscope (SEM) cross-sectional view of nanoparticles before and after pressing. Figure 2 (c-i&ii) shows the as-printed morphology, where Si nanoparticles are loosely deposited within the printed area, exhibiting high non-evenness and porosity, with averaged thickness of about 5 µm. After pressing (Figure 2d-i&ii), the nanoparticles become closely packed with thickness ~400 nm-1 µm. A clear reduction of porosity/thickness and significant improvement of flatness and uniformity are shown from the above comparison.

Laser is focused and scanned along the length direction of printed ribbons (Figure 2b) to induce melting and crystallization. Without the quartz confinement, the melted Si droplets dewet the $SiO_2$/Si substrate and form islands with contact angle in the range ~73˚ to 100˚ (Figure 2c-iii). With the confinement, it can be seen that disk-shaped islands with contact angle of ~80-90˚ were formed (Figure 2d-iii). The confining quartz largely suppresses the dewetting. Furthermore, it is noticed that melted ribbons break up into separated islands, with the size, spacing and morphology of the islands dictated by pressing pressure, laser scan speed and substrate surface properties. By increasing the pressure, the spacing between islands gradually decreases until a continuous line was formed. A clear transition from “discrete islands (break-up)” into “continuous line (no break-up)” can be observed (Figure 2e-i) when the confining gap decreases from ~1 μm to sub-500 nm. Besides the gap, it is found small linewidth (lateral confinement) forces the islands to line up along the printed trace (Figure 2e-ii) and form a linear array of islands. This indicates the location and spacing of islands can be controlled by aerosol printing parameters (length and width of the printed trace). Figure 2e-iii shows that laser scanning speed alters the size and spacing of the islands. It is found increasing laser scanning speed reduces the size of island and the spacing between islands. Slower scanning speed provides longer melt duration allowing more time for melted nanoparticles to coalescence and form large islands. In this study it is found the scanning speed in 50-70 mm/s and power 25-35 W can fully melt the ribbons and produce large islands. It is also found the islands tend to form elongated shapes on nitride surface, while on oxide surface round shaped islands are mostly found (FigureS3). The difference in island/ribbon morphology is mainly due to lower contact angle of liquid Si on nitride surface compared with that on oxide surface.

To shed lights onto the confinement effect on break-up process that determines the island size, the stability criteria of liquid thin film is re-visited. It is known for a thin, continuous and confined liquid on a substrate, the stability (no break-up) condition is when the contact angle between the liquid and bounding surface is < 90$^{o}$ [77-79]. The contact angle of liquid Si on $SiO_2$/Si substrate as observed in Figure 2d-iii satisfies this condition. However, break-up is commonly observed in current study. Recent Lattice Boltzmann Model shows the balling effect in selective laser melting (SLM) are strongly influenced by local powder arrangement[780,81]. It is then believed that the break-up condition in melted NP ribbons would critically depend on perturbation and porosity introduced by random particle packing. NP planarization reduces the perturbation and porosity which suppresses the break-up of melted NP films as observed in Figure 2(e) and Figure 3(a-d). To understand the effect of particle packing density on break-up process, Computational Fluid Dynamics (CFD) simulation of the evolution of liquid NP film bounded by two surfaces were performed (details in supplementary materials, FigureS4). The simulation results suggest that higher packing density effectively suppresses or delays break-up process and vice versa as observed in Figure 2e-i.

Based on this finding, the confining gap was varied to modulate the spacing and size of islands with laser scanning speed fixed at 70 mm/s. Figure 3 (a-d) shows the SEM morphology (i&ii) and crystallinity (ii&iv) of the laser crystallized Si islands subjected to

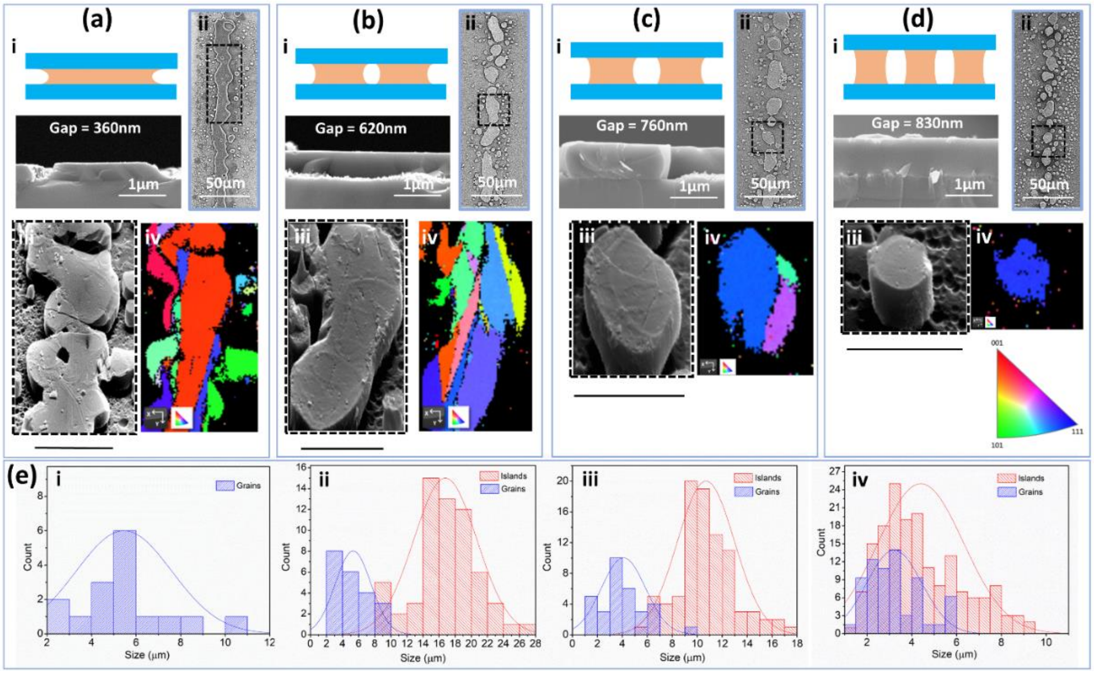

Figure 3. Influence of confining gap on the morphology and crystalline structure of annealed Si. (a) Mode I, continuous long ribbon. (b) Mode II, elongated islands. (c) Mode III, isolated islands. (d) Mode IV, single-crystal islands. (i) Schematic draw of molten Si under confinement and annealed Si thickness; (ii) SEM image of annealed Si; SEM image of zoomed in Si pattern with gran boundary revealed by Secco etching (iii) and corresponding EBSD map (iv). Scale bar for iii & iv through (a) to (d) are 10 µm. (e)The distribution of grain size and islands size for four different modes.

various confining gaps, as indicated by the SEM measured film thickness. To examine the crystallinity of these ribbons/islands, the Secco etchant was used to reveal the grain boundary in the sample[49,82] and then characterized with SEM. With the smallest gap (360 nm), the break-up was largely suppressed and a continuous long ribbon was obtained (length ≥100 µm, width ~10 µm). Grain boundaries are clearly seen indicating a polycrystal structure. Increasing the gap to 620 nm leads to elongated islands (length ~20 µm, width ~10 µm) that are isolated with no obvious grain boundaries. Further increasing of the gap left clearly isolated islands (length ~10 µm, width ~10 µm), which were dominated by a large grain and some small defects on the edges. At even larger gap, the large grain almost occupied the entire domain (~5 μm×5 μm) indicating single-crystal islands. The crystallinity of these islands were further confirmed via electron backscattering diffraction (EBSD) mapping, showing good consistance with the Secco etching results. Statistical analysis of grain size (as measured from EBSD) are presented along with the distribution of island size in Figure 3e for each confining gap. It is found with small gap, the grain size are largely less than island size while with large gap, grain size starts to overlap with island size indicating formation of single-crystal islands. Further, no obvious impurity was detected through energy-dispersive X-ray spectroscopy (EDX) in laser crystallized islands (Figure S5). Therefore, by tuning the confining gap with air cushion pressure, Si nanoparticles can be melted and crystallized into single-crystal islands.

Finally, attempts were made to transfer print as-fabricated single-crystal islands onto flexible substrates. Heterogeneous integration of high performance semiconductor materials with flexible/polymer substrates represents a key step towards realizing high-performance integrated electronics. Transfer printing has been largely employed for integration of pre-fabricated microstructured silicon ribbons, single-crystal ribbons, and nanowire devices[30-34,84] onto flexible platform. However, these devices were dominantly fabricated by IC micro-machining and subtractive methods on silicon-on-insulator (SOI) or bulk wafers. Current work suggests an additive and direct printing approach to generate pre-patterned single-crystal Si islands for transfer printing. The transfer printing process is illustrated in Figure 4(a). Firstly, as-fabricated Si islands (on 2 μm oxide) were etched using 5% HF to make under-cut. Then, the sample was thoroughly cleaned with sufficient DI water and dried with nitrogen gas flow. Subsequently, the sample was dried in Ar at 350˚C for 30 min to make the SiO$_2$ hydrophobic (allowing detachment of Polyvinyl alcohol (PVA) from SiO$_2$/Si substrate during peeling off step). Then PVA solution was coated as adhesive film on the sample to be transferred. Receiving substrates (Polyimide) was pressed gently on top of the PVA allowing fully contact of PVA films with receiving substrate. By peeling off the receiving substrate, the Si islands were transferred to the receiving substrate. The transfer printing process is shown in Figure 4a. Figure 4 shows linear array of single-crystal islands after laser crystallization (Figure 4b)

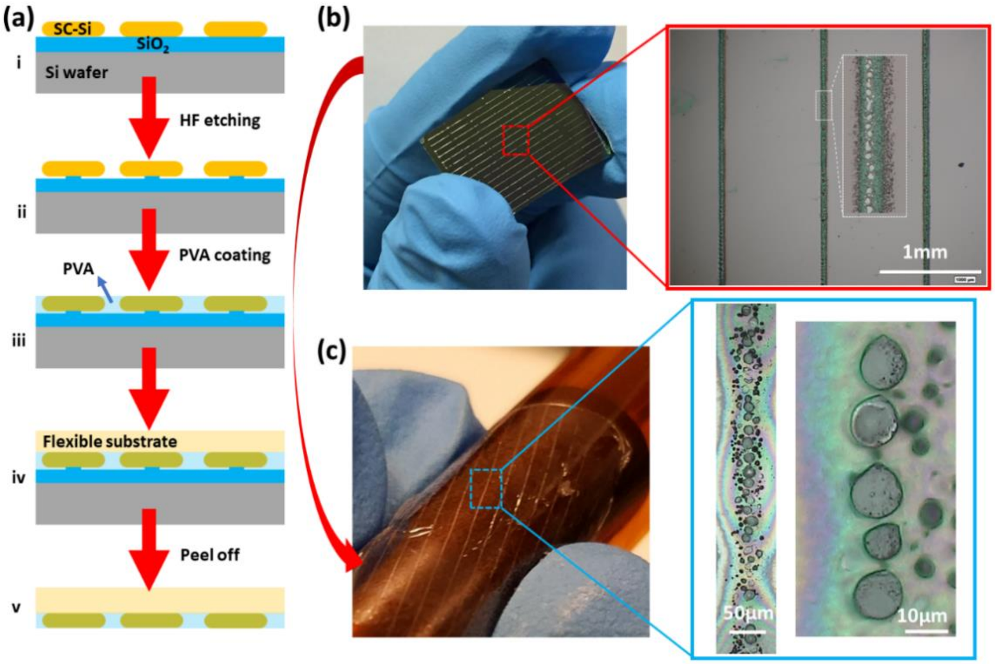

Figure 4. Transfer of fabricated single-crystal Si islands. (a) Schematic of detailed transfer procedure. i. As fabricated Si on wafer with 2 µm thermal oxide layer; ii. Under-cut making using HF etching; iii. Coating of adhesive PVA layer; iv. Flexible substrate attachment; v. Peel off with Si islands on flexible substrate. Photography and optical image of fabricated single-crystal Si islands (b) before and (c) after transfer on flexible substrate.

and after being transferred to a plastic substrate (Figure 4c). The transferred single crystal islands can be potentially used for flexible thin-film transistor (TFT) arrays after fabrication of electrodes[30-32,84-86].

## 3. CONCLUSIONS

In summary, we have demonstrated a scalable additive scheme to fabricate single-crystal Si structures via aerosol printing, planarization and confined laser crystallization. Here, aerosol printing offers a mask-free, high-efficiency approach for direct Si patterning at microscales. The confining (and pressing) system significantly planarizes and densifies the printed Si patterns. Millisecond laser crystallization of the confined Si nanoparticles leads to the formation of single-crystal islands of ~5µm wide and <1µm thick. Furthermore, the as-fabricated single-crystal Si islands were successfully transferred onto flexible substrates.

## 4. MATERIALS AND METHODS

**Si ink:** Different from previous Si printing[21,22], binder-free Si ink was developed here. The Si nanopowders have an average size of 30 nm, which is provided by Advanced Chemicals Supplier (purity of >99.99%). Silicon nanopowders were mixed with methanol and ethanol in weight ratio of 1:9:90. Typically, 0.4 g of Si nanopowders, 3.6 g of methanol, and 36 g of ethanol were used. After mixing, the solution was sonicated for 10 min twice with a 10 min gap before printing.

**Other materials:** Quartz slide was purchased from Ted Pella, which is made from high purity fused quartz (with a nominal softening point of 1683˚C). Silicon wafer with 2 µm thermal oxide was provided by University Wafer. A customized inflatable airbag was bought from MatJack Inc. to planarize the Si nanoparticles with uniform pressure. More details can be found in supplementary materials.

**Laser Parameters:** A single mode ytterbium fiber laser (IPG, 1065 nm, CW, 100 W) was directed into a galvanometer for high speed (up to 800 mm $s^{-1}$) laser sintering. A defocused laser spot with diameter of ~80 µm was selected to cover the whole printed Si line. Typically, sintering was conducted with laser power of ~35 W and scanning speed of 70 mm/s. The laser crystallization is performed with an in-situ pressing/planarization system (details in supplementary materials).

**Characterization**: SEM images and EDX analysis were taken in Hitachi S-4700 or Helios Nanolab 600. EBSD mapping were conducted in Helios Nanolab 600. An FEI F20 instrument was used for transmission electron microscope (TEM) image.

**Secco etching**: Mixture of HF (48%) and $K_2Cr_2O_7$ solution (44 g $K_2Cr_2O_7$ dissolved in 1 L of $H_2O$, or 0.15 M) in a ratio of 2:1 were prepared as the original etchant. One part of the original etchant was freshly diluted with 4 parts of distilled water to etch the crystallized Si sample. A typical moderate etching time of 45 seconds was used[82].

## ACKNOWLEDGEMENTS

The work is supported by the collaborative NSF Grant CMMI-1363392 and 1363313 to C.G. and H.P. This research was also partially supported Intelligent System Center (ISC) and Material Research Center (MRC) at Missouri University of Science and Technology and ORAU Ralph E. Powe Junior Faculty Enhancement Award. Their financial supports are greatly appreciated.

## REFERENCES

(1) Rogers, J. A.; Someya, T.; Huang, Y. Materials and Mechanics for Stretchable Electronics. *Science* **2010**, *327*, 1603-1607.

(2) Yin, Z.; Huang, Y.; Bu, N.; Wang, X.; Xiong, Y. Inkjet Printing for Flexible Electronics: Materials, Processes and Equipments. *Chinese Sci. Bull.* **2010**, *55*, 3383-3407.

(3) Yu, X.; Mahajan, K. B.; Shou, W.; Pan, H. Materials, Mechanics, and Patterning Techniques for Elastomer-Based Stretchable Conductors. *Micromachines* **2017**, 8, 7

(4) Mohammed, M. G.; Kramer, R. All-Printed Flexible and Stretchable Electronics. *Adv. Mater.* **2017**, *29*, 1604965.

(5) Rim, Y. S.; Bae, S.-H.; Chen, H.; De Marco, N.; Yang, Y. Recent Progress in Materials and Devices toward Printable and Flexible Sensors. *Adv. Mater.* **2016**, *28*, 4415-4440.

(6) Yu, X.; Shou, W.; Mahajan, B. K.; Huang, X.; Pan, H. Materials, Processes, and Facile Manufacturing for Bioresorbable Electronics: A Review. *Adv. Mater.* **2018**, *30*, 1707624.

(7) Ko, S. H.; Pan, H.; Grigoropoulos, C. P.; Luscombe, C. K.; Fréchet, J. M. J.; Poulikakos, D. All-Inkjet-Printed Flexible Electronics Fabrication on a Polymer Substrate by Low-Temperature High-Resolution Selective Laser Sintering of Metal Nanoparticles. *Nanotechnology* **2007**, *18*, 345202.

(8) Ko, S. H.; Pan, H.; Grigoropoulos, C. P.; Luscombe, C. K.; Fréchet, J. M. J.; Poulikakos, D. Air Stable High Resolution Organic Transistors by Selective Laser Sintering of Ink-Jet Printed Metal Nanoparticles. *Appl. Phys. Lett.* **2007**, *90*, 141103.

(9) Ko, S. H.; Chung, J.; Pan, H.; Grigoropoulos, C. P.; Poulikakos, D. Fabrication of Multilayer Passive and Active Electric Components on Polymer Using Inkjet Printing and Low Temperature Laser Processing. *Sensors Actuators A Phys.* **2007**, *134*, 161-168.

(10) Bade, S. G. R.; Li, J.; Shan, X.; Ling, Y.; Tian, Y.; Dilbeck, T.; Besara, T.; Geske, T.; Gao, H.; Ma, B. Fully Printed Halide Perovskite Light-Emitting Diodes with Silver Nanowire Electrodes. *ACS Nano* **2015**, *10*, 1795-1801.

(11) Kordás, K.; Mustonen, T.; Tóth, G.; Jantunen, H.; Lajunen, M.; Soldano, C.; Talapatra, S.; Kar, S.; Vajtai, R.; Ajayan, P. M. Inkjet Printing of Electrically Conductive Patterns of Carbon Nanotubes. *Small* **2006**, *2*, 1021-1025.

(12) Small, W. R.; in het Panhuis, M. Inkjet Printing of Transparent, Electrically Conducting Single-walled Carbon-nanotube Composites. *Small* **2007**, *3*, 1500-1503.

(13) Okimoto, H.; Takenobu, T.; Yanagi, K.; Miyata, Y.; Shimotani, H.; Kataura, H.; Iwasa, Y. Tunable Carbon Nanotube Thin-Film Transistors Produced Exclusively via Inkjet Printing. *Adv. Mater.* **2010**, *22*, 3981-3986.

(14) Torrisi, F.; Hasan, T.; Wu, W.; Sun, Z.; Lombardo, A.; Kulmala, T. S.; Hsieh, G.-W.; Jung, S.; Bonaccorso, F.; Paul, P. J. Inkjet-Printed Graphene Electronics. *ACS Nano* **2012**, *6*, 2992-3006.

(15) Li, Y.; Gao, T.; Yang, Z.; Chen, C.; Luo, W.; Song, J.; Hitz, E.; Jia, C.; Zhou, Y.; Liu, B. 3D-Printed, All-in-One Evaporator for High-Efficiency Solar Steam Generation under 1 Sun Illumination. *Adv. Mater.* **2017**, *29*, 1700981.

(16) Garnier, F.; Hajlaoui, R.; Yassar, A.; Srivastava, P. All-Polymer Field-Effect Transistor Realized by Printing Techniques. *Science* **1994**, *265*, 1684-1686.

(17) Li, J.; Zhao, Y.; Tan, H. S.; Guo, Y.; Di, C.A.; Yu, G.; Liu, Y.; Lin, M.; Lim, S. H.; Zhou, Y. A Stable Solution-Processed Polymer Semiconductor with Record High-Mobility for Printed Transistors. *Sci. Rep.* **2012**, *2*, 754.

(18) Minari, T.; Kanehara, Y.; Liu, C.; Sakamoto, K.; Yasuda, T.; Yaguchi, A.; Tsukada, S.; Kashizaki, K.; Kanehara, M. Room-Temperature Printing of Organic Thin-Film Transistors with π-Junction Gold Nanoparticles. *Adv. Funct. Mater.* **2014**, *24*, 4886-4892.

(19) Ridley, B. A.; Nivi, B.; Jacobson, J. M. All-Inorganic Field Effect Transistors Fabricated by Printing. *Science* **1999**, *286*, 746-749.

(20) Shimoda, T.; Matsuki, Y.; Furusawa, M.; Aoki, T.; Yudasaka, I.; Tanaka, H.; Iwasawa, H.; Wang, D.; Miyasaka, M.; Takeuchi, Y. Solution-Processed Silicon Films and Transistors. *Nature* **2006**, *440* (7085), 783.

(21) Härting, M.; Zhang, J.; Gamota, D. R.; Britton, D. T. Fully Printed Silicon Field Effect Transistors. *Appl. Phys. Lett.* **2009**, *94*, 193509.

(22) Sani, N.; Robertsson, M.; Cooper, P.; Wang, X.; Svensson, M.; Ersman, P. A.; Norberg, P.; Nilsson, M.; Nilsson, D.; Liu, X. All-Printed Diode Operating at 1.6 GHz. *Proc. Natl. Acad. Sci.* **2014**, *111*, 11943-11948.

(23) Takeya, J.; Yamagishi, M.; Tominari, Y.; Hirahara, R.; Nakazawa, Y.; Nishikawa, T.; Kawase, T.; Shimoda, T.; Ogawa, S. Very High-Mobility Organic Single-Crystal Transistors with in-Crystal Conduction Channels. *Appl. Phys. Lett.* **2007**, *90*,102120.

(24) Minemawari, H.; Yamada, T.; Matsui, H.; Tsutsumi, J.; Haas, S.; Chiba, R.; Kumai, R.; Hasegawa, T. Inkjet Printing of Single-Crystal Films. *Nature* **2011**, *475*, 364.

(25) Kim, Y.; Yoo, B.; Anthony, J. E.; Park, S. K. Controlled Deposition of a High-performance Small-molecule Organic Single-crystal Transistor Array by Direct Ink-jet Printing. *Adv. Mater.* **2012**, *24*, 497–502.

(26) Park, K. S.; Cho, B.; Baek, J.; Hwang, J. K.; Lee, H.; Sung, M. M. Single-Crystal Organic Nanowire Electronics by Direct Printing from Molecular Solutions. *Adv. Funct. Mater.* **2013**, *23*, 4776-4784.

(27) Rigas, G.-P.; Payne, M. M.; Anthony, J. E.; Horton, P. N.; Castro, F. A.; Shkunov, M. Spray Printing of Organic Semiconducting Single Crystals. *Nat. Commun.* **2016**, *7*, 13531.

(28) Lee, L.; Baek, J.; Park, K. S.; Lee, Y.-E.; Shrestha, N. K.; Sung, M. M. Wafer-Scale Single-Crystal Perovskite Patterned Thin Films Based on Geometrically-Confined Lateral Crystal Growth. *Nat. Commun.* **2017**, *8*, 15882.

(29) Gu, Z.; Wang, K.; Li, H.; Gao, M.; Li, L.; Kuang, M.; Zhao, Y. S.; Li, M.; Song, Y. Direct-Writing Multifunctional Perovskite Single Crystal Arrays by Inkjet Printing. *Small* **2017**, *13*, 1603217.

(30) Menard, E.; Nuzzo, R. G.; Rogers, J. A. Bendable Single Crystal Silicon Thin Film Transistors Formed by Printing on Plastic Substrates. *Appl. Phys. Lett.* **2005**, *86*, 93507.

(31) Ahn, J.-H.; Kim, H.-S.; Lee, K. J.; Jeon, S.; Kang, S. J.; Sun, Y.; Nuzzo, R. G.; Rogers, J. A. Heterogeneous Three-Dimensional Electronics by Use of Printed Semiconductor Nanomaterials. *Science* **2006**, *314*, 1754-1757.

(32) Meitl, M. A.; Zhu, Z.-T.; Kumar, V.; Lee, K. J.; Feng, X.; Huang, Y. Y.; Adesida, I.; Nuzzo, R. G.; Rogers, J. A. Transfer Printing by Kinetic Control of Adhesion to an Elastomeric Stamp. *Nat. Mater.* **2006**, *5*, 33.

(33) Khang, D.-Y.; Jiang, H.; Huang, Y.; Rogers, J. A. A Stretchable Form of Single-Crystal Silicon for High-Performance Electronics on Rubber Substrates. *Science* **2006**, *311*, 208-212.

(34) Baca, A. J.; Meitl, M. A.; Ko, H. C.; Mack, S.; Kim, H.; Dong, J.; Ferreira, P. M.; Rogers, J. A. Printable Single-crystal Silicon Micro/nanoscale Ribbons, Platelets and Bars Generated from Bulk Wafers. *Adv. Funct. Mater.* **2007**, *17*, 3051-3062.

(35) Wagner, R. S.; Ellis, W. C. Vapor-liquid-solid Mechanism of Single Crystal Growth. *Appl. Phys. Lett.* **1964**, *4*, 89-90.

(36) Chen, K.; Kapadia, R.; Harker, A.; Desai, S.; Kang, J. S.; Chuang, S.; Tosun, M.; Sutter-Fella, C. M.; Tsang, M.; Zeng, Y. Direct Growth of Single-Crystalline III-V Semiconductors on Amorphous Substrates. *Nat. Commun.* **2016**, *7*, 10502.

(37) Im, J. S.; Sposili, R. S.; Crowder, M. A. Single-Crystal Si Films for Thin-Film Transistor Devices. *Appl. Phys. Lett.* **1997**, *70*, 3434-3436.

(38) Yuan, H.-C.; Ma, Z.; Roberts, M. M.; Savage, D. E.; Lagally, M. G. High-Speed Strained-Single-Crystal-Silicon Thin-Film Transistors on Flexible Polymers. *J. Appl. Phys.* **2006**, *100*, 13708.

(39) Zhao, J.; Wang, A.; Green, M. A.; Ferrazza, F. 19.8% Efficient “honeycomb” Textured Multicrystalline and 24.4% Monocrystalline Silicon Solar Cells. *Appl. Phys. Lett.* **1998**, *73*, 1991-1993.

(40) Yoshikawa, K.; Kawasaki, H.; Yoshida, W.; Irie, T.; Konishi, K.; Nakano, K.; Uto, T.; Adachi, D.; Kanematsu, M.; Uzu, H. Silicon Heterojunction Solar Cell with Interdigitated Back Contacts for a Photoconversion Efficiency over 26%. *Nat. Energy* **2017**, *2*, 17032.

(41) Ji, X.; Lei, S.; Yu, S.-Y.; Cheng, H. Y.; Liu, W.; Poilvert, N.; Xiong, Y.; Dabo, I.; Mohney, S. E.; Badding, J. V. Single-Crystal Silicon Optical Fiber by Direct Laser Crystallization. *ACS Photonics* **2016**, *4*, 85-92.

(42) Evers, J.; Klüfers, P.; Staudigl, R.; Stallhofer, P. Czochralski’s Creative Mistake: A Milestone on the Way to the Gigabit Era. *Angew. Chemie Int. Ed.* **2003**, *42*, 5684-5698.

(43) Im, J. S.; Kim, H. J.; Thompson, M. O. Phase Transformation Mechanisms Involved in Excimer Laser Crystallization of Amorphous Silicon Films. *Appl. Phys. Lett.* **1993**, *63*, 1969–1971.

(44) Chimmalgi, A.; Hwang, D. J.; Grigoropoulos, C. P. Nanoscale Rapid Melting and Crystallization of Semiconductor Thin Films. *Nano Lett.* **2005**, *5*, 1924–1930.

(45) Taheri, M. L.; McGowan, S.; Nikolova, L.; Evans, J. E.; Teslich, N.; Lu, J. P.; LaGrange, T.; Rosei, F.; Siwick, B. J.; Browning, N. D. In Situ Laser Crystallization of Amorphous Silicon: Controlled Nanosecond Studies in the Dynamic Transmission Electron Microscope. *Appl. Phys. Lett.* **2010**, *97*, 32102.

(46) Saboundji, A.; Mohammed-Brahim, T.; Andrä, G.; Bergmann, J.; Falk, F. Thin Film Transistors on Large Single Crystalline Regions of Silicon Induced by CW Laser Crystallization. *J. Non. Cryst. Solids* **2004**, *338*, 758-761.

(47) Andrä, G.; Bergmann, J.; Falk, F. Laser Crystallized Multicrystalline Silicon Thin Films on Glass. *Thin Solid Films* **2005**, *487*, 77-80.

(48) Michaud, J. F.; Rogel, R.; Mohammed-Brahim, T.; Sarret, M. CW Argon Laser Crystallization of Silicon Films: Structural Properties. *J. Non. Cryst. Solids* **2006**, *352*, 998–1002.

(49) Park, S. J.; Ku, Y. M.; Kim, K. H.; Kim, E. H.; Choo, B. K.; Choi, J. S.; Kang, S. H.; Lim, Y. J.; Jang, J. CW Laser Crystallization of Amorphous Silicon; Dependence of Amorphous Silicon Thickness and Pattern Width on the Grain Size. *Thin Solid Films* **2006**, *511*, 243–247.

(50) Said-Bacar, Z.; Prathap, P.; Cayron, C.; Mermet, F.; Leroy, Y.; Antoni, F.; Slaoui, A.; Fogarassy, E. CW Laser Induced Crystallization of Thin Amorphous Silicon Films Deposited by EBE and PECVD. *Appl. Surf. Sci.* **2012**, *258*, 9359-9365.

(51) Amkreutz, D.; Müller, J.; Schmidt, M.; Hänel, T.; Schulze, T. F. Electron-beam Crystallized Large Grained Silicon Solar Cell on Glass Substrate. *Prog. Photovoltaics Res. Appl.* **2011**, *19*, 937–945.

(52) Sameshima, T.; Kaneko, Y.; Andoh, N. Rapid Joule Heating of Metal Films Used to Crystallize Silicon Films. *Appl. Phys. A* **2002**, *74*, 719-723.

(53) In, J. Bin; Xiang, B.; Hwang, D. J.; Ryu, S.-G.; Kim, E.; Yoo, J.-H.; Dubon, O.; Minor, A. M.; Grigoropoulos, C. P. Generation of Single-Crystalline Domain in Nano-Scale Silicon Pillars by near-Field Short Pulsed Laser. *Appl. Phys. A* **2014**, *114*, 277–285.

(54) Shou, W.; Pan, H. Silicon-Wall Interfacial Free Energy via Thermodynamics Integration. *J. Chem. Phys.* **2016**, *145*, 184702.

(55) Gibbons, J. F.; Lee, K. F.; Magee, T. J.; Peng, J.; Ormond, R. CW Laser Recrystallization Of< 100> Si on Amorphous Substrates. *Appl. Phys. Lett.* **1979**, *34*, 831–833.

(56) Xiang, B.; Hwang, D. J.; In, J. Bin; Ryu, S.-G.; Yoo, J.-H.; Dubon, O.; Minor, A. M.; Grigoropoulos, C. P. In Situ TEM near-Field Optical Probing of Nanoscale Silicon Crystallization. *Nano Lett.* **2012**, *12*, 2524–2529.

(57) Wang, L.; Rho, Y.; Shou, W.; Hong, S.; Kato, K.; Eliceiri, M.; Shi, M.; Grigoropoulos, C. P.; Pan, H.; Carraro, C. Programming Nanoparticles in Multiscale: Optically Modulated Assembly and Phase Switching of Silicon Nanoparticle Array. *ACS Nano* **2018**, *12*, 2231–2241.

(58) Pan, H.; Shou, W. Single Crystal Formation in Micro/nano-Confined Domains by Melt-Mediated Crystallization without Seeds. *J. Phys. D. Appl. Phys.* **2015**, *48*, 225302.

(59) Liu, Y.; Deal, M. D.; Saraswat, K. C.; Plummer, J. D. Single-Crystalline Si on Insulator in Confined Structures Fabricated by Two-Step Metal-Induced Crystallization of Amorphous Si. *Appl. Phys. Lett.* **2002**, *81*, 4634-4636.

(60) Hara, A.; Yoshino, K.; Takeuchi, F.; Sasaki, N. Selective Single-Crystalline-Silicon Growth at the Pre-Defined Active Region of a Thin Film Transistor on Glass by Using Continuous Wave Laser Irradiation. *Jpn. J. Appl. Phys.* **2003**, *42*, 23.

(61) Arora, H.; Du, P.; Tan, K. W.; Hyun, J. K.; Grazul, J.; Xin, H. L.; Muller, D. A.; Thompson, M. O.; Wiesner, U. Block Copolymer Self-Assembly–directed Single-Crystal Homo-and Heteroepitaxial Nanostructures. *Science* **2010**, *330*, 214-219.

(62) Kim, D. K.; Jeong, W. H.; Bae, J. H.; Hwang, T. H.; Roh, N. S.; Kim, H. J. Selective Area Crystallization of Amorphous Silicon Using Micro-Patterned $SiO_2$ Capping Layer. *J. Cryst. Growth* **2010**, *312*, 2335-2338.

(63) Schade, M.; Mchedlidze, T.; Kittler, M.; Leipner, H. S. Light Induced Crystallization of an Amorphous Silicon Film Embedded between Silicon Oxide Layers. *Phys. status solidi* **2014**, *251*, 439-445.

(64) Danielson, D. T.; Sparacin, D. K.; Michel, J.; Kimerling, L. C. Surface-Energy-Driven Dewetting Theory of Silicon-on-Insulator Agglomeration. *J. Appl. Phys.* **2006**, *100*, 83507.

(65) Cheynis, F.; Bussmann, E.; Leroy, F.; Passanante, T.; Müller, P. Dewetting Dynamics of Silicon-on-Insulator Thin Films. *Phys. Rev. B* **2011**, *84*, 245439.

(66) Bussmann, E.; Cheynis, F.; Leroy, F.; Müller, P.; Pierre-Louis, O. Dynamics of Solid Thin-Film Dewetting in the Silicon-on-Insulator System. *New J. Phys.* **2011**, *13*, 43017.

(67) Aouassa, M.; Favre, L.; Ronda, A.; Maaref, H.; Berbezier, I. The Kinetics of Dewetting Ultra-Thin Si Layers from Silicon Dioxide. *New J. Phys.* **2012**, *14*, 63038.

(68) Grigoropoulos, C. P. *Transport in Laser Microfabrication: Fundamentals and Applications*; Cambridge University Press, 2009.

(69) Son, Y.; Yeo, J.; Moon, H.; Lim, T. W.; Hong, S.; Nam, K. H.; Yoo, S.; Grigoropoulos, C. P.; Yang, D.-Y.; Ko, S. H. Nanoscale Electronics: Digital Fabrication by Direct Femtosecond Laser Processing of Metal Nanoparticles. *Adv. Mater.* **2011**, *23*, 0935-9648.

(70) Hong, S.; Yeo, J.; Kim, G.; Kim, D.; Lee, H.; Kwon, J.; Lee, H.; Lee, P.; Ko, S. H. Nonvacuum, Maskless Fabrication of a Flexible Metal Grid Transparent Conductor by Low-Temperature Selective Laser Sintering of Nanoparticle Ink. *ACS Nano* **2013**, *7*, 5024–5031.

(71) Lee, D.; Paeng, D.; Park, H. K.; Grigoropoulos, C. P. Vacuum-Free, Maskless Patterning of Ni Electrodes by Laser Reductive Sintering of NiO Nanoparticle Ink and Its Application to Transparent Conductors. *ACS Nano* **2014**, *8*, 9807–9814.

(72) Shou, W.; Mahajan, B. K.; Ludwig, B.; Yu, X.; Staggs, J.; Huang, X.; Pan, H. Low-Cost Manufacturing of Bioresorbable Conductors by Evaporation–Condensation-Mediated Laser Printing and Sintering of Zn Nanoparticles. *Adv. Mater.* **2017**, *29*, 0935–9648.

(73) Gao, H.; Tan, H.; Zhang, W.; Morton, K.; Chou, S.Y. Air cushion press for excellent uniformity, high yield, and fast nanoimprint across a 100 mm field. *Nano Lett.* **2006**, 6, 2438-2441.

(74) Ewsuk, K.G.; Ellerby, D.T.; DiAntonio, C.B. Analysis of nanocrystalline and microcrystalline ZnO sintering using master sintering curves. *J Am Ceram Soc.* **2006**, 89(6), 2003-2009.

(75) Schwarz, S.; Thron, A.M.; Rufner, J.; van Benthem, K.; Guillon, O. Low temperature sintering of nanocrystalline zinc oxide: effect of heating rate achieved by field assisted sintering/spark plasma sintering. *J Am Ceram Soc.* **2012**, 95(8), 2451-2457.

(76) Heckel, R.W. Density-pressure relationships in powder compaction. *Trans Metall Soc AIME* **1961**, 221(4), 671-675.

(77) Chen, H.; Amirfazli, A.; Tang, T. Modeling Liquid Bridge between Surfaces with Contact Angle Hysteresis. *Langmuir* **2013**, *29*, 3310–3319.

(78) Luo, C.; Heng, X.; Xiang, M. Behavior of a Liquid Drop between Two Nonparallel Plates. *Langmuir* **2014**, *30*, 8373–8380.

(79) Shi, Z.; Zhang, Y.; Liu, M.; Hanaor, D. A. H.; Gan, Y. Dynamic Contact Angle Hysteresis in Liquid Bridges. *Colloids Surfaces A Physicochem. Eng. Asp.* **2018**, *555*, 365–371.

(80) Gusarov, A. V; Smurov, I. Modeling the Interaction of Laser Radiation with Powder Bed at Selective Laser Melting. *Phys. Procedia* **2010**, *5*, 381–394.

(81) Körner, C.; Attar, E.; Heinl, P. Mesoscopic Simulation of Selective Beam Melting Processes. *J. Mater. Process. Technol.* **2011**, *211*, 978-987.

(82) Zheng, C. Innovation in Photovoltaic Science, Engineering, and Policy: A Potential Trillion-Dollar Global Industry for Sustainable Energy. UC Berkeley 2014.

(83) Falk, F.; Andrä, G. Laser Crystallization-a Way to Produce Crystalline Silicon Films on Glass or on Polymer Substrates. *J. Cryst. Growth* **2006**, *287*, 397–401.

(84) Mack, S.; Meitl, M. A.; Baca, A. J.; Zhu, Z.-T.; Rogers, J. A. Mechanically Flexible Thin-Film Transistors That Use Ultrathin Ribbons of Silicon Derived from Bulk Wafers. *Appl. Phys. Lett.* **2006**, *88*, 213101.

(85) Briseno, A. L.; Mannsfeld, S. C. B.; Ling, M. M.; Liu, S.; Tseng, R. J.; Reese, C.; Roberts, M. E.; Yang, Y.; Wudl, F.; Bao, Z. Patterning Organic Single-Crystal Transistor Arrays. *Nature* **2006**, *444*, 913.

(86) Mannsfeld, S. C. B.; Sharei, A.; Liu, S.; Roberts, M. E.; McCulloch, I.; Heeney, M.; Bao, Z. Highly Efficient Patterning of Organic Single-Crystal Transistors from the Solution Phase. *Adv. Mater.* **2008**, *20*, 4044-4048.

# SUPPLEMENTAL INFORMATION

## Aerosol printing

A home-built aerosol printer was used for Si ink printing. Aerosol printing was completed using pneumatic nebulizers to aerosolize the Si ink. The aerosol was focused by nozzle for direct printing of ribbons. The linewidth generally decreases with the increase of printing speed, in the range of 20-100 µm. The smallest continuous line printed in our study was about 20 µm.

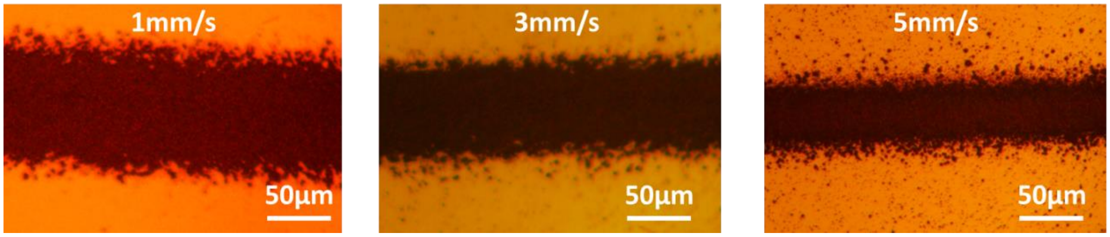

Figure S1. The influence of printing speed on printed linewidth.

## Confined crystallization system

In order to realize confined crystallization, a confined laser processing setup was developed as shown in Figure S2. An IPG Fiber Laser (1065 nm, CW, 100W) was directed into a galvanometer (laser scanner) for high speed laser sintering and crystallization. A defocused laser spot with diameter of ~80 µm was selected to cover the whole printed Si line. A broadband precision window (provided by ThorLabs) was used

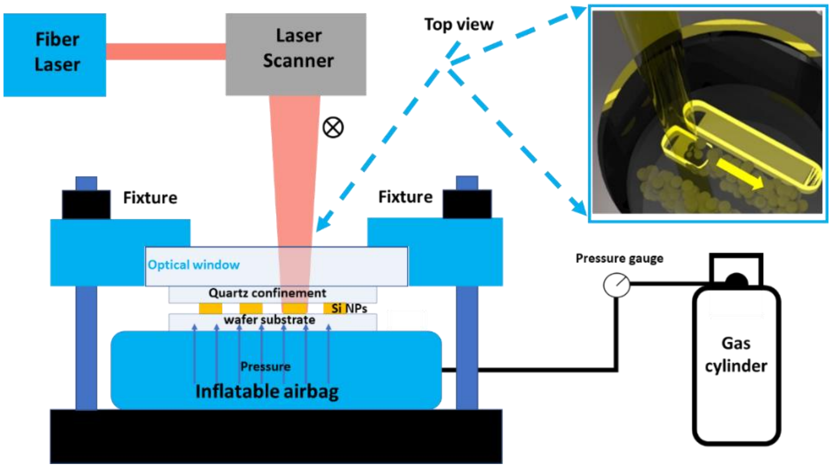

Figure S2. Schematics of confined laser processing setup. (Inset shows the laser moving direction, along the printed Si line)

as the optical window, allowing the laser pass through and directly contacting the quartz confinement. The optical window was assembled with a mechanical fixture system, which fixs the up side of the processing setup. A quartz slide was purchased from Ted Pella, which is made from high purity fused quartz (with a nominal softening point of 1683˚C), was used as the confinement. Silicon wafer with 2 μm thermal oxide was provided by University Wafer and used as the substrate. A customized inflatable airbag was bought from MatJack Inc. to planarize the Si nanoparticles with uniform pressure (up to 120 psi). The assembling sequence from bottom to up is airbag, wafer substrate (with Si NPs line on it), quartz confinement, and optical window. By inflating the airbag through a gas cylinder, where a pressure gauge was used to monitor the pressure, pressure can be applied from the bottom of the wafer to planarized the Si NPs. The applied pressure can be adjusted up 120 psi, typically, 100, 110, 115, and 120 psi were used. The laser scanned along the line as shown in the inset of Figure S2.

## Substrate effects on ribbon morphology

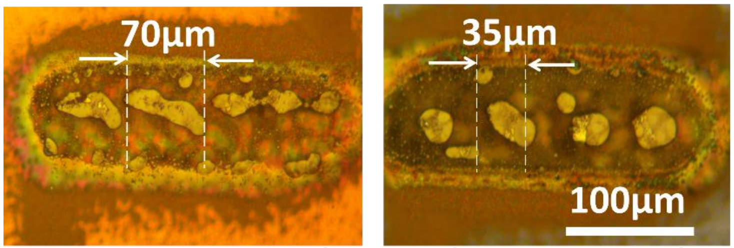

**Low contact angle substrate (nitride)**

**High contact angle substrate (oxide)**

Figure S3. Ribbon morphology on different substrates.

## Computational Fluid Dynamics simulation

A Finite Difference Method (FDM) numerical computation of the full Navier-Stokes equation based on the volume-of-fluid (VoF) interface tracking method is used to simulate the evaluation of liquid ribbon process. This method has been recently applied to reproduce the Rayleigh-Plateau instability for nano- and microscale liquid filaments [Hartnett2015; Ubal2014]. Wall-adhesion model is invoked to model contact angles. Navior’s slip condition has been included. The commercial software FLUENT is employed to perform the simulation.

To consider the particle packing, the initial particle configuration is obtained from a separate Discrete Element Modeling (DEM) where NP packing have been simulated (as shown in Figure S4). With this model, the instability as a function of powder density can be studied. In the 2D simulation, nanoparticles with diameter ~500 nm were packed to different packing density as controlled by the gap distance. In the simulation, the nanoparticles were set to be melted (liquid) at t=0 s. Simulations (Figure S4-b) show that with 62.5% powder packing density, the film breaks up into several segments within 1.75 μs with contact angle 80º (<90º). By increasing packing density to 74.5%, break-up is largely suppressed as shown by continuous stripe after 12.3 μs. The simulation indicates the break-up can be suppressed or delayed by increasing powder packing density.

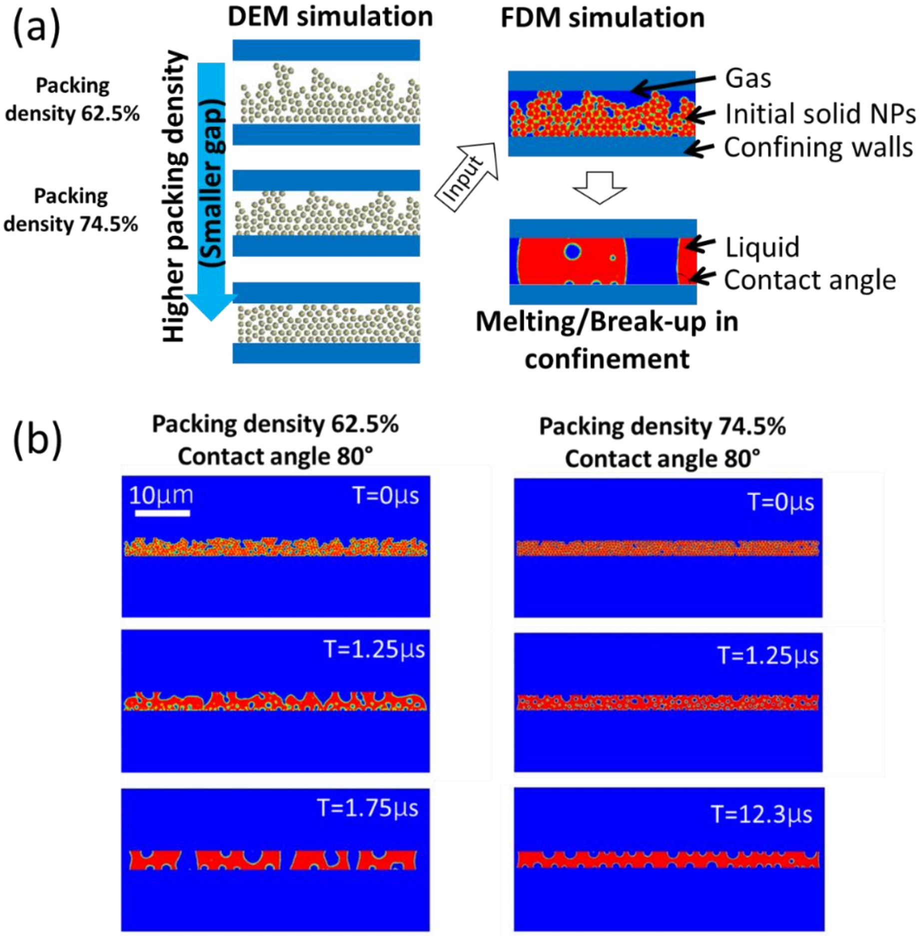

Figure S4. Simulation scheme to study break-up of melted nanoparticles in confined configuration.

## Energy-dispersive X-ray (EDX) spectroscopy characterization

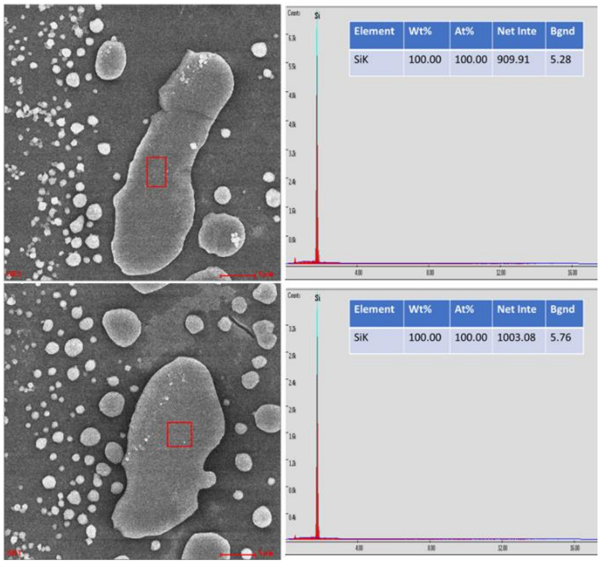

Figure S5. EDX analysis of representative sintered Si islands.

In order to examine the elemental composition of crystallized Si islands, EDX analysis were conducted on randomly selected islands. Tiny peaks for oxygen were observed, however, the software was not able to identify such small percentage, giving a 100% of Si. Thus, it was concluded that no obvious impurity was detected.

## Transfer method

We developed a transfer printing method to print the as-fabricated single-crystal islands onto flexible substrates for potential application of flexible electronic component. The detailed procedure is described below: (i) First, the Si pattern (on 2 μm thermal dioxide) was etched using 5% HF to make under-cut. The etching time can be adjusted accordingly for different patterns. (ii) Then, the sample with under-cut was cleaned with sufficient DI water and dried with nitrogen gas flow. Subsequently, the sample was dried

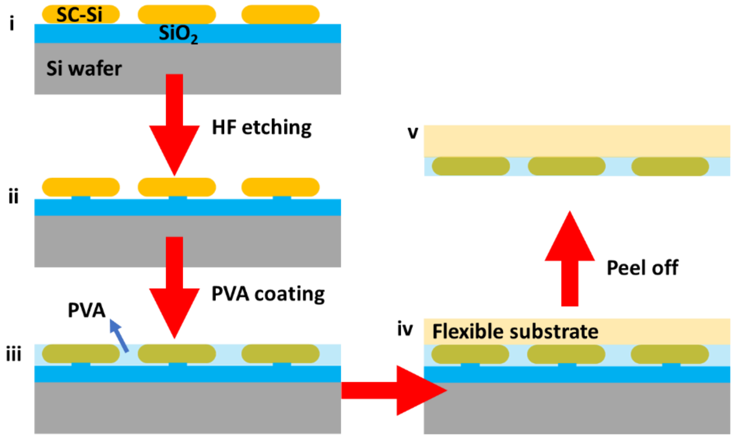

Figure S6. The procedure for Si transfer.

in Ar at 350 ˚C for 30 min (allowing detachment of Polyvinyl alcohol (PVA) from $SiO_2$/Si during peeling off). (iii) 10 wt% PVA solution was then spin-coated using speed of 500 rpm on the sample to be transferred, followed with 110˚C baking for 3 min. (iv) Then flexible substrate (polyimide) can be used as receiving substrate on the top PVA film. (v) Then the Si sample covered with PVA film and supported with flexible substrate can be peeled off from the edge.

## References

[1]. Hartnett, Chris A., et al. "Instability of nano- and microscale liquid metal filaments: Transition from single droplet collapse to multidroplet breakup." Langmuir 31.50 (2015): 13609-13617.

[2]. Ubal, Sebastián, et al. "The influence of inertia and contact angle on the instability of partially wetting liquid strips: A numerical analysis study." Physics of Fluids 26.3 (2014): 032106.

# SECTION

## 2. CONCLUSIONS

In this work, firstly, the interfacial energies of a Si system in contact with flat and structured walls were computed by molecular dynamics (MD) simulations. The thermodynamics integration (TI) method was implemented in Tersoff potentials for Si and $SiO_2$ system. The calculated interfacial energies were employed to predict the nucleation mechanisms in a slab of liquid silicon confined by two walls and compared with MD simulation results. We found that (1) For flat wall, the liquid-flat wall interfacial energy increases with confining pressure, and $\gamma_{cw}$-$\gamma_{lw}$ decreases monotonically with increasing confining pressure. With low confining pressure, $\gamma_{cw}$-$\gamma_{lw}$ is close to $\gamma_{lc}$, indicating nucleation originating from the interface (or heterogeneous nucleation) is not energetically favored. Namely, in the free surface nucleation, nucleation is not originated from the free surface. (2) For structured $SiO_2$ wall, $\gamma_{cw}$-$\gamma_{lw}$ is found to be 0.209 $J/m^2$, lower than $\gamma_{lc}$ ~0.29-0.43 $J/m^2$, suggesting that heterogeneous nucleation tends to happen when molten Si solidifies in contact with $SiO_2$ Substrate. This hypothesis was proved by direct simulating Si crystallization on $SiO_2$.

Then, the obtained results from MD were used in our phenomenological model. It is found that small domain size is critical to increase the probability of forming single crystals. The heating pulse (laser) width needs to be optimized for confined crystallization. In domain size ≥100nm, nanosecond laser pulse (≤100ns) is incapable to form single crystals, which agrees with experimental observations. It is suggested that in order to manufacture micro-sized single crystal Si in contact with substrate, a continuous-wave (CW) laser is needed in a scanning mode.

To examine our theoretical prediction, crystallization of Si using CW laser was conducted. In order to reduce the cost and increase the throughput of single crystal Si manufacturing, a printing approach was proposed to prepare the micro-scale Si pattern using aerosol printer. Then, a pressing system was designed and used to densify and planarize the printed Si. Followed with laser melting and crystallization in a confined domain, single crystal silicon micro/nanoribbons were successfully fabricated. Further, a transfer method was developed to transfer the as fabricated high quality crystalline Si to flexible substrate for device fabrication.

Based on our experimental results, the following conclusions can be drawn:

(1) Aerosol printing is an effective way to pattern Si nanoparticles in microscale, which can be used for laser crystallization. Such printing approach is capable for large scale fabrication.

(2) The pressing (or confining) system can not only densify and planarize the Si pattern, but also modulate the structure and crystallinity of the sintered Si through adjusting the confinement gap.

(3) Preventing heat dissipation and reducing the cooling rate is the right approach to realize micro-size single crystal Si fabrication.

# 3. FUTURE WORK

Based on the conclusions and experience gained from this work, various valuable research can be conducted in the area of laser crystallization and other printing-based manufacturing. Followings are some directions suggested for future study:

(1) Chemical-reaction-based crystallization of silicon [24] (and other semiconductor materials) should be explored.

(2) Better patterning technique, such as lithography, can be used for clean and well-defined pattern preparation, which can offer higher probability to form single crystal ribbon.

(3) Laser-induced forward transfer (LIFT) can be used to direct write single-crystal Si (or Ge) arrays [25]. This additive strategy can possibly build 3D crystalline structures for 3D micro-electronics. Some molecular dynamics (MD) simulation results indicate that the crystallization can be finished during fly with good chance of single crystal nanoparticle formation. The crystallized nanoparticles can then be landed on receiving substrate avoiding high temperature damage to flexible substrate with low melting point.

(4) It is realized from our MD crystallization simulations that crystallization for large domain (>100nm) of Si or Ge should make use of other simulation techniques, such as phase field simulation, which can handle more realistic situations.

(5) Confinement (or pressing) can be applied to other area to overcome dewetting problems, such as uniform film preparation, and porosity reduction. The thermodynamics phenomena of molten Si and associated solidification process should

be further studied to get better understanding. It is believed that the pressing procedure can also inspire powder-bed-based 3D printing to prepare objects with reduced voids/porosity and enhanced mechanical performance.

## REFERENCES

[1].Im, James S., H. J. Kim, and Michael O. Thompson. "Phase transformation mechanisms involved in excimer laser crystallization of amorphous silicon films." Applied Physics Letters 63.14 (1993): 1969-1971.

[2].Im, James S., Robert S. Sposili, and M. A. Crowder. "Single-crystal Si films for thin-film transistor devices." Applied physics letters 70.25 (1997): 3434-3436.

[3].Chimmalgi, A., Hwang, D.J. and Grigoropoulos, C.P., 2005. Nanoscale rapid melting and crystallization of semiconductor thin films. Nano letters, 5(10), pp.1924-1930.

[4].Taheri, M.L., McGowan, S., Nikolova, L., Evans, J.E., Teslich, N., Lu, J.P., LaGrange, T., Rosei, F., Siwick, B.J. and Browning, N.D., 2010. In situ laser crystallization of amorphous silicon: Controlled nanosecond studies in the dynamic transmission electron microscope. Applied Physics Letters, 97(3), p.032102.

[5].Saboundji, A., Mohammed-Brahim, T., Andrä, G., Bergmann, J. and Falk, F., 2004. Thin film transistors on large single crystalline regions of silicon induced by cw laser crystallization. Journal of non-crystalline solids, 338, pp.758-761.

[6].Andrä, G., Bergmann, J. and Falk, F., 2005. Laser crystallized multicrystalline silicon thin films on glass. Thin Solid Films, 487(1), pp.77-80.

[7].Michaud, J.F., Rogel, R., Mohammed-Brahim, T. and Sarret, M., 2006. CW argon laser crystallization of silicon films: structural properties. Journal of non-crystalline solids, 352(9), pp.998-1002.

[8].Park, S.J., Ku, Y.M., Kim, K.H., Kim, E.H., Choo, B.K., Choi, J.S., Kang, S.H., Lim, Y.J. and Jang, J., 2006. CW laser crystallization of amorphous silicon; dependence of amorphous silicon thickness and pattern width on the grain size. Thin solid films, 511, pp.243-247.

[9].Said-Bacar, Z., Prathap, P., Cayron, C., Mermet, F., Leroy, Y., Antoni, F., Slaoui, A. and Fogarassy, E., 2012. CW laser induced crystallization of thin amorphous silicon films deposited by EBE and PECVD. Applied Surface Science, 258(23), pp.9359-9365.

[10].K. Fujiwara, K. Maeda, H. Koizumi, J. Nozawa, and S. Uda, J. Appl. Phys. 112, 113521 (2012).

[11].Apte, Pankaj A., and Xiao Cheng Zeng. "Anisotropy of crystal-melt interfacial free energy of silicon by simulation." Applied Physics Letters 92.22 (2008): 221903.

[12].Shao, Y., and F. Spaepen. "Undercooling of bulk liquid silicon in an oxide flux." Journal of applied physics 79.6 (1996): 2981-2985.

[13].Liu, R. P., T. Volkmann, and D. M. Herlach. "Undercooling and solidification of Si by electromagnetic levitation." Acta materialia 49.3 (2001): 439-444.

[14].Stiffler, S. R., Michael O. Thompson, and P. S. Peercy. "Supercooling and nucleation of silicon after laser melting." Physical review letters 60.24 (1988): 2519.

[15].Evans, P. V., and S. R. Stiffler. "Interfacial atomic transport in the nucleation of crystalline silicon from the melt." Acta metallurgica et materialia 39.11 (1991): 2727-2731.

[16].Li, D., and D. M. Herlach. "High undercooling of bulk molten silicon by containerless processing." EPL (Europhysics Letters) 34.6 (1996): 423.

[17].Zeng, X. C., and D. Stroud. "The solid-liquid interfacial tension of diamond-structure Si and Ge." Journal of Physics: Condensed Matter 1.9 (1989): 1779.

[18].Tang, Yuk Wai, Jun Wang, and Xiao Cheng Zeng. "Molecular simulations of solid-liquid interfacial tension of silicon." The Journal of chemical physics 124.23 (2006): 236103.

[19].Evers, Jürgen, et al. "Czochralski's creative mistake: a milestone on the way to the gigabit era." Angewandte Chemie International Edition 42.46 (2003): 5684-5698.

[20].Khang, Dahl-Young, et al. "A stretchable form of single-crystal silicon for high-performance electronics on rubber substrates." Science 311.5758 (2006): 208-212.

[21].Baca, Alfred J., et al. "Printable single ‐ crystal silicon micro/nanoscale ribbons, platelets and bars generated from bulk wafers." Advanced Functional Materials 17.16 (2007): 3051-3062.

[22].Wagner, R. S., and W. C. Ellis. "Vapor-liquid-solid mechanism of single crystal growth." Applied Physics Letters 4.5 (1964): 89-90.

[23].Chen, Kevin, et al. "Direct growth of single-crystalline III-V semiconductors on amorphous substrates." Nature communications 7 (2016): 10502.

[24].Shimoda, Tatsuya, et al. "Solution-processed silicon films and transistors." Nature 440.7085 (2006): 783.

[25].Zywietz, Urs, et al. "Laser printing of silicon nanoparticles with resonant optical electric and magnetic responses." Nature communications 5 (2014): 3402.

# VITA

Wan Shou was born in Zhejiang Province, China, 1990. He received a Bachelor of Engineering in Textile Engineering from Tianjin Polytechnic University, China, in June 2012. He graduated in the summer of 2014 with a Master of Science in Mechanical Engineering, from the University of Louisiana at Lafayette. He joined the graduate program in Mechanical Engineering at Missouri University of Science and Technology (Missouri S&T) in the fall of 2014. He worked under Dr. Heng Pan at Missouri S&T for the last four years as a Research Assistant. In December 2018, he received his Doctor of Philosophy in Mechanical Engineering from Missouri University of Science and Technology, Rolla, Missouri, USA. During his Ph.D. study, he authored and co-authored 12 journal papers and 2 conference papers.